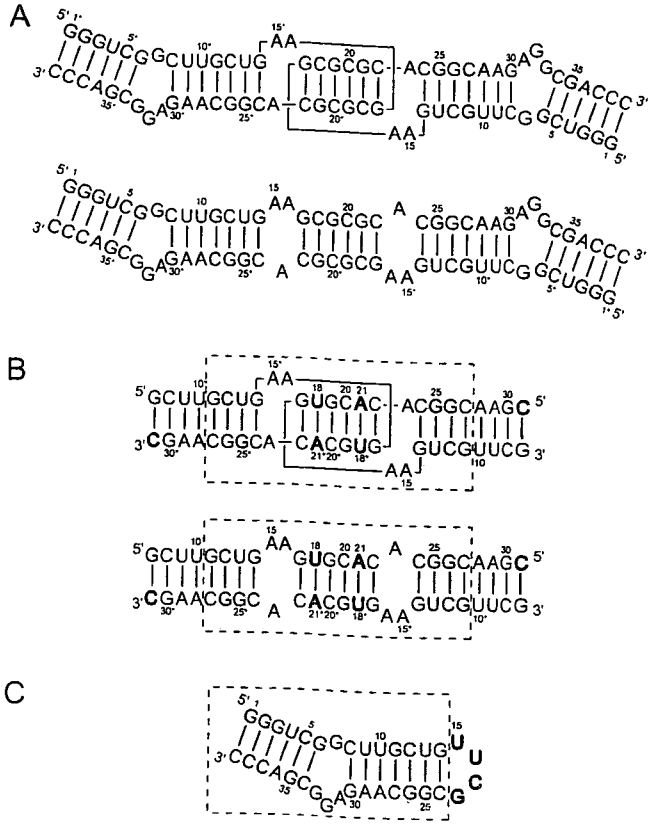

Fig. 1. **Secondary structure of a 39mer RNA corresponding to the dimerization initiation site (DIS39) and its fragments used in this study.** (A) The kissing-loop and extended-duplex dimers of DIS39. (B) The kissing-loop and extended-duplex dimers of loop25, which is composed of the loop and stem of DIS39. Modified residues are indicated by open characters. The sequence of the self-complementary loop was modified to increase the dispersion of NMR signals, and a base pair was added to the stem. The broken box indicates the part to be used for structure calculation. (C) Bulge34 consists of the stem-bulge-stem region of DIS39 and the connecting UUCG loop. The broken box indicates the part to be used for structure calculation. Gray shading indicates the two base pairs, C12–G26 and U13–G25, that are superimposed to combine the structures of the kissing-loop or extended-duplex dimer region and the stem-bulge-stem region. Asterisks indicate residues in the other strand.

MATERIALS AND METHODS

RNA Synthesis, Purification and Preparation—Non-labeled loop25 was synthesized chemically by the phosphoramidite method with an automatic DNA/RNA synthesizer, Expedite model 8909 (PerSeptive Biosystems Inc., MA, USA). The protection groups were removed with ammonia and tetra-*n*-butylammonium fluoride. Non-labeled DIS39 and bulge34 were synthesized enzymatically by the *in vitro* transcription reaction method with AmpliScribe T7 transcription kits (Epicentre Technologies Co., WI, USA). Purification for each RNA sample was performed by PAGE using 30 cm × 40 cm glass plates (Nihon Eido Co. Ltd., Tokyo, Japan) under denaturing conditions, and extensive desalting by ultrafiltration (Centricon YM3, Amicon Inc., MA, USA) was carried out. For stable isotopic labeling by the *in vitro* transcription with ^{13}C- and ^{15}N-labeled NTPs (Nippon Sanso, Tokyo, Japan), we used DIS39 rather than shorter loop25 and bulge34 because the efficiency of *in vitro* transcription is better for larger RNA.

For the preparation of the kissing-loop dimer, DIS39 or loop25 in water was incubated at 368 K for 5 min and chilled on ice for 5 min. Then, the solvent was adjusted to 1× PN-buffer [10 mM sodium phosphate (pH 7.0) and 50 mM NaCl] by adding concentrated buffer. For the preparation of the extended-duplex dimer, DIS39 or loop25 in 1× PN-buffer was incubated at 368 K for 5 min and slowly cooled to room temperature. Bulge34 was annealed by heating at 363 K for 5 min and snap-cooling on ice. To confirm the formation of the hairpin structure, the samples were subjected to a native PAGE experiment. For NMR measurements, RNA samples were dissolved in 10 mM sodium phosphate buffer (pH 7.0) containing 50 mM NaCl. The final concentration of chemically synthesized loop25 was 1.8 mM. The concentrations of DIS39 and bulge34 (transcripts) were 1.0 and 0.5 mM, respectively. The concentration of the kissing-loop and extended-duplex dimers of [G-^{13}C/^{15}N] and [A-^{13}C/^{15}N] DIS39 were 0.4, 0.3, 0.2 and 0.1 mM, respectively.

NMR Measurements—NMR spectra were recorded on Bruker DRX-500 and DRX-600 spectrometers. Spectra were recorded at probe temperatures of 283 to 303 K and NMR data at 298 K were used for structure calculation. The imino proton signal of the G and U residues in H_2O were distinguished from each other by the HSQC selected and HSQC filtered 1D spectra measured with ^{13}C and ^{15}N-labeled DIS39. Exchangeable proton NOEs were determined by 2D NOESY in H_2O with a mixing time of 150 ms using the jump-and-return scheme and gradient pulses for water suppression. For resonance assignments, well-established procedures were used (*30*). The H2 protons of adenosine were assigned based on a 2D HSQC experiment with natural abundance ^{13}C. NOE distance restraints from non-exchangeable protons were obtained from 2D NOESY experiments (mixing times of 50, 100, 200, and 400 ms) in D_2O. The intensities of the NOEs between exchangeable protons were interpreted as distances of 2.1–5.0 Å. For loop25, distances were estimated by analyzing the initial slope of NOE intensities for mixing times of 25, 50, 100, 200 ms. Judgment of intermolecular NOE is described in the result section. Two restraints (>5 Å) were added to the distance restraints based on the absence of NOE cross peaks in the case of the kissing-loop dimer. For bulge34, the intensities of NOEs due to nonexchangeable protons were interpreted as distances with a margin of −1.5 to +1.5 Å for the 100 ms 2D NOESY and −1.0 to +2.0 Å for the 200 ms 2D NOESY. Two restraints (>5 Å) were added to the distance restraints based on the absence of NOE cross peaks. The formation of hydrogen binding of G:C, A:U or G:U base pairs is interpreted as distance constraints as 1.8–2.1 Å for hydrogen and acceptor atoms and 2.8–3.2 Å for donor and acceptor atoms; G11:C27 to G14:C24, G11*:C27* to G14*:C24* and G17:C22* to C22:G17* for loop25 in the kissing-loop dimer, G11:C27* to G14:C24*, G11*:C27 to G14*:C24 and G17:C22* to C22:G17* for loop25 in the extended-duplex dimer, and G1:C39 to C5:G35 and U9:A29 to G14:C24 for bulge34. Dihedral restraints were obtained as described below. The absence of crosspeaks between H1′–H2′ in the 2D TOCSY and DQF-COSY experiments was interpreted as the residue being in the C3′-*endo*

conformation. On the other hand, the presence of strong crosspeaks between H1′–H2′ in the 2D TOCSY and DQF-COSY experiments was interpreted as the residue being in the C2′-*endo* conformation. The correction of sugar puckering is interpreted as dihedral restraints for ν_2 as 40.00 ± 20.00° (C3′-*endo*) or −35.00 ± 20.00° (C2′-*endo*). Based on the sequential connectivity of the Watson-Crick and G-U base pairs, the RNA-A conformation was assumed for the stem region and dihedral restraints were introduced for backbone torsion angles (α, β, γ, δ, ε and ζ) as the ideal conformation with a margin of ±10.00°. For loop25 in the kissing-loop dimer, information about the C3′-*endo* conformation (G11–G14, G17–C27), the C2′-*endo* conformation (A16) and RNA-A conformation in the stem region (G11–U13, U18–A21, G25–C27) was used as the dihedral restraints. For loop25 of the extended-duplex dimer, information about the C3′-*endo* conformation (G11–G14, G17-C27) and RNA-A conformation in the stem region (G11–U13, U18–A21, G25–C27) was used as the dihedral restraints. For bulge34, the information about the C3′-*endo* conformation (G1–G14, C24–A31, C34–C39) and RNA-A conformation in the stem region (G1–C5, G11–G14, C24–C27, G35–C39) was used as the dihedral restraints.

Structure Calculation—A set of 100 structures was calculated using the simulated annealing protocol described below with the InsightII/Discover package, and the amber force field was used. The force constants were 100 kcal mol^{-1} $Å^{-2}$ for distance restraints and 100 kcal mol^{-1} rad^{-2} for dihedral restraints. The starting coordinates were randomized, and the randomized structures were heated to 2,000 K in 5 ps, and the temperature was kept to 2,000 K for another 5 ps. After that, all restraints were increased to full values in 20 ps, then, decreased to 1/10 of full values in 5 ps at 2,000 K. Van der Waals radii were increased from 0.1 to 0.825 in 20 ps at 2,000 K. All restraints were increased to full value again in 10 ps at 2,000 K. Scalings for non-bond interactions were increased to full value in the next 20 ps at 2,000 K, and the temperature was kept to 2,000 K for another 5 ps. Then, the temperature was gradually scaled to 300 K in 10 ps. After that, the structure was heated from 300 to 1,000 K in 5 ps, and the van der Waals radii were increased from 0.825 to 1 at 1,000 K, and then decreased from 1 to 0.825 at 1,000 K. An additional 5 ps of dynamics was performed at 1,000 K, and the temperature was gradually scaled to 300 K for 10 ps. A final minimization step was performed, which included a Lennard-Jones potential and electrostatic terms with a dielectric constant of 7. The ten final structures with the lowest total energies were chosen.

RESULTS AND DISCUSSION

Analysis of the NMR Spectra of DIS39, Loop25 and Bulge34—Our previous NMR study revealed that the two types of dimers of DIS39 prepared as described in "MATERIALS AND METHODS" correspond to the kissing-loop and extended-duplex dimers (*31*). NMR spectra of DIS39 in each of the kissing-loop and extended-duplex dimers were measured in D_2O, and the signals due to H1′, H6/H8 were assigned by the sequential assignment method (Fig. 2). Figure 3A shows the difference in the chemical shift of H1′, H6/H8 between the two types of dimers. It was found that the difference is concentrated in the loop region. Interestingly, structures of the stem-bulge-stem region of the kissing-loop and extended-duplex dimers were extremely similar, even though the stems are formed by intra and inter molecules. This was also shown by analysis of the TOCSY spectrum; differences are located in the loop regions. Most residues were adapted to the C3′-*endo* conformation except for G32, G33 in the bulge-out region of both forms, A16 in the kissing-loop dimer and A15, A16 in the extended-duplex dimer, which might be a mixture of the C2′-*endo* and C3′-*endo* conformations.

To reveal further authentic structure, two RNA molecules were designed; loop25 includes the loop region and bulge34 includes the stem-bulge-stem region (Fig. 1, B and C). Loop25 was constructed to determine the authentic structure of the loop region. In order to increase the dispersion of the NMR signals, the sequence of the loop was modified from GCGCGC to GUGCAC. One base pair was added by replacing A31 by C31 in the stem to increase the stability of the kissing-loop dimer. It is noted that the loop sequences of GCGCGC and GUGCAC correspond to those of HIV-1 subtypes B and F (*32*), respectively, and both sequences have dimerization activity (*6*, *9*, *10*). The chemical shifts of loop25 were compared with those of DIS39 in each of the kissing-loop and extended-duplex dimers (Fig. 3, B and C). For both conformations, the chemical shifts for most of the stem region and A15, A16 and A23 were strikingly similar between the loop25 and DIS39. Due to the base alterations, the chemical shifts of the self complement loop were slightly different for both dimers. The chemical shift of H8 was shifted more than 0.2 ppm due to the addition of the terminal base pair. It is noteworthy that the chemical shift difference in loop25 between the kissing-loop and extended-duplex dimers (Fig. 3D) was almost identical to that of DIS39 (Fig. 3A). These results indicate that the structures of loop25 in the kissing-loop and extended-duplex dimers are essentially identical to those of DIS39. Upon analysis of the TOCSY spectrum, it was found that most of the residues were adapted to the C3′-*endo* conformation except A15 and A16 for the extended duplex dimer and A16 for the kissing loop dimer, and these results also agree with the results for DIS39.

Bulge34 was constructed to determine the authentic structure of the stem-bulge-stem region. Bulge34 consists of the stem-bulge-stem region of DIS39 and the connecting UUCG loop. The NMR signals of bulge34 were assigned by the sequential assignment technique. The chemical shift of H1′, H6/H8 of bulge34 were compared to those of DIS39 in the kissing-loop dimer (Fig. 3E). The chemical shifts for the stem-bulge-stem regions of bulge34 and DIS39 were identical, although the chemical shifts of the residues adjacent to the loop were slightly different by reflecting the difference in the closing loop sequences. Upon analysis of the TOCSY spectrum, it was found that most residues were adapted to the C3′-*endo* conformation except for G32, G33 in the bulge-out region and C in the UUCG loop, and that the conformation in the stem-bulge-stem region also agreed with that of DIS39. These results indicate that the structure of the stem-bulge-stem region of bulge34 is identical to that of DIS39.

Thus, the structures of DIS39 for two types of dimers can be determined by determining the structures of loop25 and bulge34, and combining them.

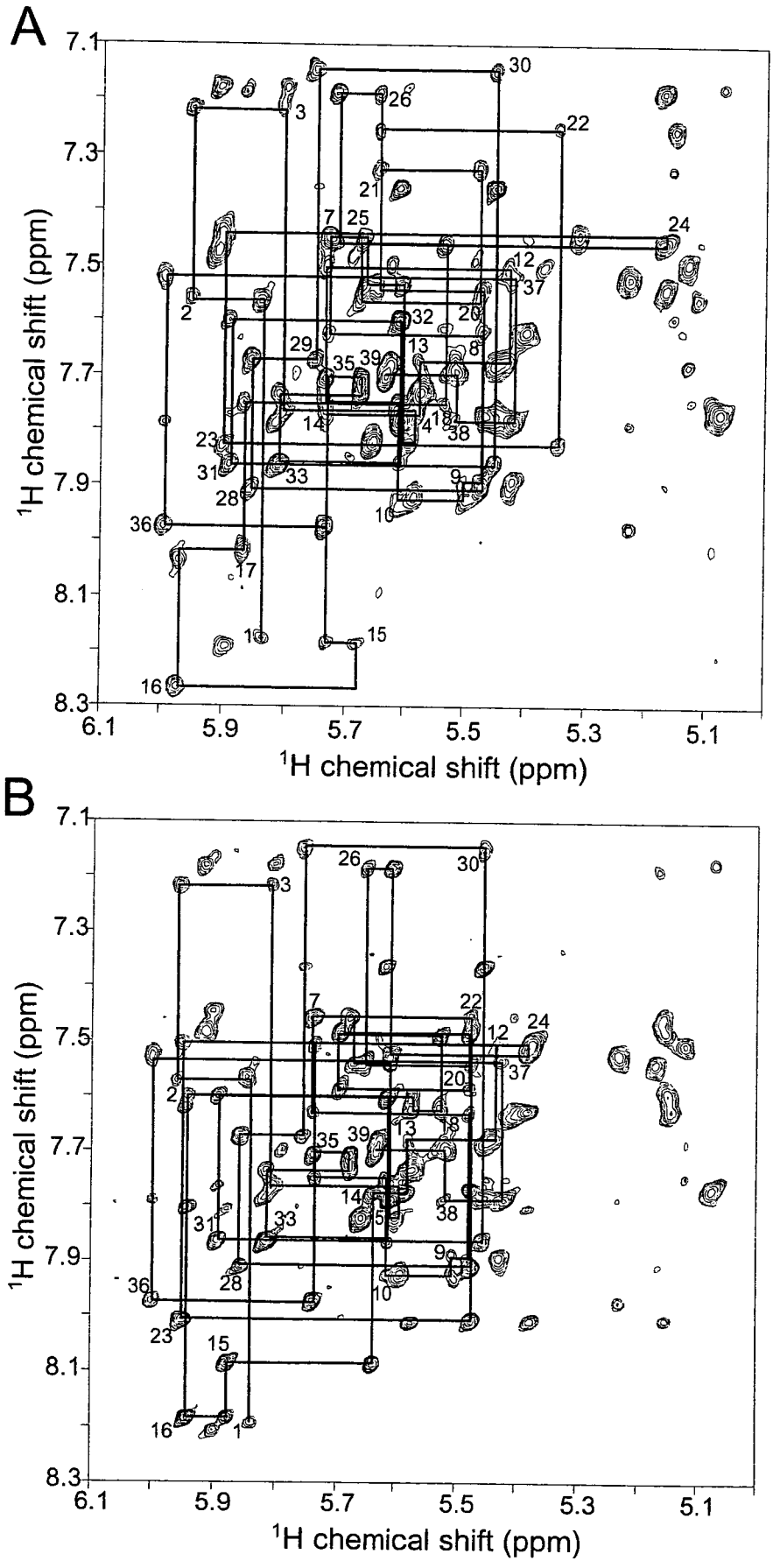

Fig. 2. **2D NOESY spectra of the (A) kissing-loop and (B) extended-duplex dimers of DIS39 measured in D_2O at 25°C with a mixing time of 200 ms.** Cross-peaks between aromatic H6/H8 protons and ribose H1′ protons are shown, and the sequential NOE connectivity is indicated.

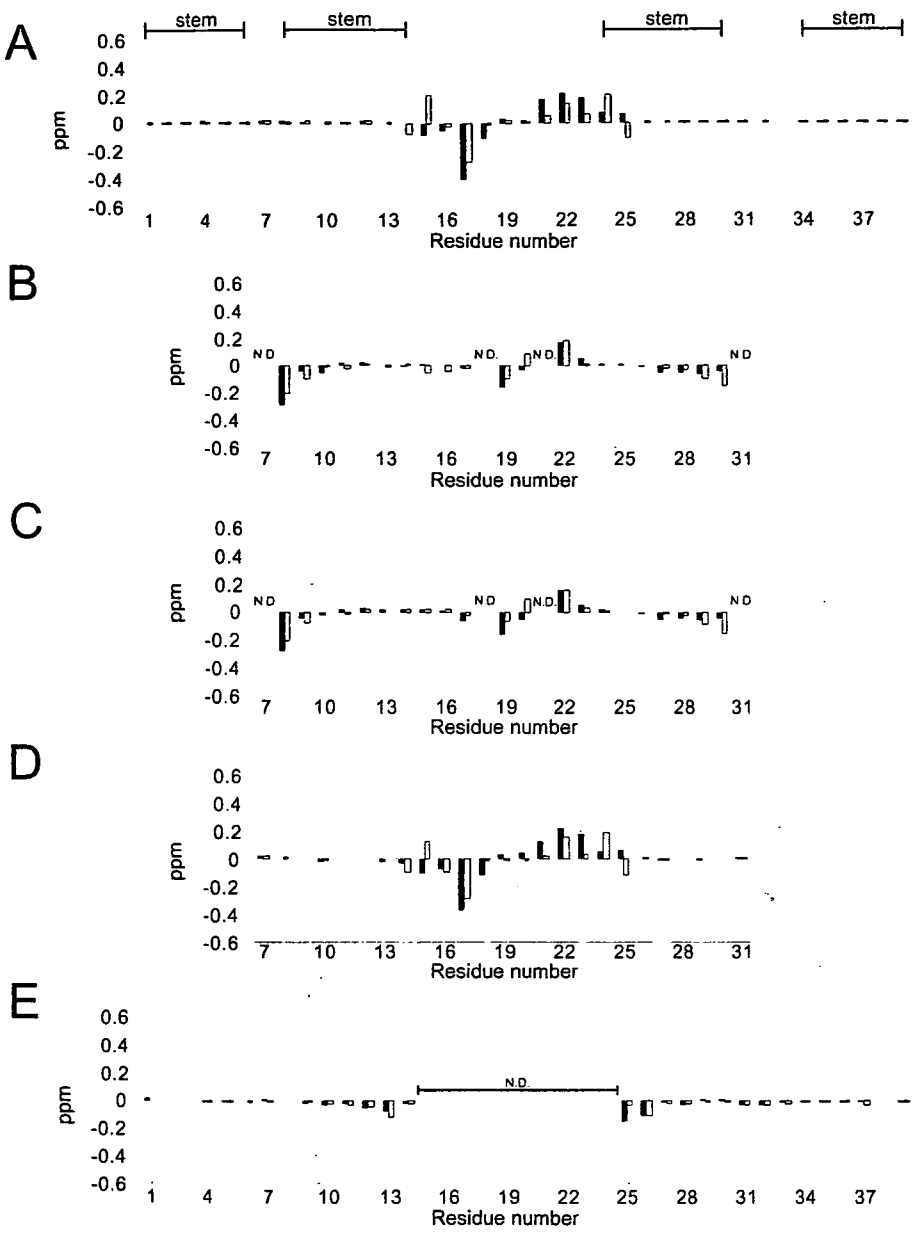

Fig. 3. Chemical shift differences for H6/H8 and H1′. Filled and open bars indicate H6/H8 and H1′, respectively. (A) Chemical shift differences between the kissing-loop and extended-duplex dimers of DIS39. Lines above the graph indicate the stem regions. (B) Chemical shift differences between DIS39 and loop25 in the kissing-loop dimer (data for replaced residues 7, 18, 21 and 31 are not shown). (C) Chemical shift differences between DIS39 and loop25 in the extended-duplex dimer (data for replaced residues 7, 18, 21 and 31 are not shown). (D) Chemical shift differences between the kissing-loop and extended-duplex dimers of loop25. (E) Chemical shift differences between DIS39 and bulge34 in the kissing-loop dimer (data for residues 15–24 are not shown).

Structure Determination—The loop region of loop25 in the kissing-loop dimer: To determine the structure of the loop region of DIS39 in both the kissing-loop and extended-duplex dimers, the NMR signals of loop25 were further analyzed and structural information was collected. The structure of the loop region consisting of the nine nucleotide loop and the stem with four base pairs was determined as shown by the broken box in Fig. 1B. A total of 286 distance restraints, 76 hydrogen bonding distance restraints, 140 dihedral restraints (Table 1), and 136 chiral restraints were used for the structural calculation. Three NOEs in the loop region, H2(A21)–H1′(U18), H2(A21)–H1′(G19) and H2(A21)–H8(G19), were judged to be intermolecular by analysis of the imino proton spectra. Four NOEs in the stem-loop linking region were considered to be intermolecular or intramolecular based on the results of the isotope filter NMR measurement (data not shown), and it was concluded that two NOEs, H2(A23)–H1′ (G17), H2(A16)–H1′ (G16), are intermolecular and three NOE, H8(A16)–H1′ (A16), H8(A16)–H2′ (A16), are intramolecular. One NOE in the stem-loop linking region was considered to be intermolecular or intramolecular in the structure calculation, and it was concluded that this NOE, H2(A23)–H2(A15), is intramolecular. Each restraint is used twice for two molecules. The structures were calculated by the restrained molecular dynamic calculation with the simulated annealing method. The structure was defined with a heavy atom r.m.s.d. of 2.14 Å for the ten converged structures (Fig. 4A, left panel), and the minimized average structure is shown in Fig. 4A (right panel). Although the overall convergence was not very good, the self-complementary region was well defined with 0.76 Å, and the stem-loop linking region was defined with 1.86 Å. The structural statistics are summarized in Table 1.

The loop region of loop25 in the extended-duplex dimer: The loop region of loop25 in the extended-duplex dimer was

Table 1. **NMR restraints and structural statistics.**

	Number of restraints		
	loop25 in the kissing-loop dimer (17 mer × 2)	loop25 in the extended-duplex dimer (17 mer × 2)	bulge34 (30 mer)
Distance restraints	286	384	345
imino-imino	12	12	10
intra residue	154	182	163
intra molecule	106	174	170
inter molecule	12	16	–
>5 Å	2	0	2
Hydrogen bonding distance restraints	76	76	58
Dihedral restraints	140	138	126
3′-*endo*	30	30	28
2′-*endo*	2	0	0
RNA-A stems	108	108	98
r.m.s.d. from the idealized geometry (Å)			
Bonds (Å)	0.00897 ± 0.00004	0.00803 ± 0.00020	0.00775 ± 0.00015
Angle (°)	2.43 ± 0.23	2.33 ± 0.05	2.24 ± 0.07
Impropers (°)	1.57 ± 0.10	1.82 ± 0.64	1.53 ± 0.21
Heavy-atoms r.m.s.d. (Å)[a]			
All	2.14	1.45	1.98
Stem-loop linking region[b]	1.86	1.31	
Bulge region[c]			1.90

[a]Averaged r.m.s.d. between an average structure and the 10 converged structures were calculated. The converged structures did not contain experimental distance violations >0.2 Å or dihedral violations >5°, [b]The stem-loop linking region consists of residues 14 to 17, 22 to 24, 14* to 17* and 22* to 24*, [c]The bulge region consists of residues 6 to 10 and 28 to 34. Asterisks indicate residues in the other molecule.

determined (broken box in Fig. 1B). A total of 384 distance restraints, 76 hydrogen bonding distance restraints, 138 dihedral restraints (Table 1) and 136 chiral restraints were used for the structure calculation. For the stem-loop linking region, H2 of A23 was connected by intermolecular NOEs to H1′ and H2 of A15, H2 of A16 and H1′ of G17. The structures were calculated by the restrained molecular dynamic calculation with the simulated annealing method described above. The structure was well defined with a heavy atom r.m.s.d. of 1.45 for the ten converged structures (Fig. 4B, left panel), and the minimized average structure is shown in Fig. 4B (right panel). The stem-loop linking region was defined with 1.31 Å. The structural statistics are summarized in Table 1.

The stem-bulge-stem region of bulge34: A structural determination was performed for bulge34 except for the UUCG loop (broken box in Fig. 1C). A total of 345 distance restraints, 58 hydrogen bonding distance restraints, 126 dihedral restraints (Table 1) and 120 chiral restraints were used for the structure calculation. Two NOE restraints (>5 Å), H2(A31)–H1′(U9) and H1′(A31)–H1′(U9), were added to the distance restraints based on the absence of NOE cross peaks. The structures were calculated by the restrained molecular dynamic calculation with a simulated annealing protocol. The structure was defined with a heavy atom r.m.s.d. of 1.98 for the ten converged structures (Fig. 4C, left panel), and the minimized average structure is shown in Fig. 4C (right panel). Although the overall convergence is not very good, the stem regions are well defined with 0.83 or 0.78 Å, respectively. The bulge region was defined with 1.90 Å. The structural statistics are summarized in Table 1.

The two types of dimers of DIS39: Solution structures of DIS39 were then constructed by combining the structure parts. The structures of the kissing-loop or extended-duplex dimer region and stem-bulge-stem region were combined by superimposing two base pairs, C12:G26 and U13:G25 (Fig. 1, gray area). The left panels of Fig. 5 show the ten structures prepared by using the minimized average structure of the stem-bulge-stem region (Fig. 4C, right) and each of the ten lowest energy structures of the loop region (Fig. 4, A or B, left) superimposed by the loop region. The right panels of Fig. 5 show the structures prepared using the minimized average structure of the stem-bulge-stem region (Fig. 4C, right) and the loop region (Fig. 4, A or B, right). The relative angles between the stem-bulge-stem regions differ between the kissing-loop and extended-duplex dimers as shown in the right panels of Fig. 5. However, the fluctuations of the relative angles are rather large and the ranges overlap between the two dimers as shown in the left panels of Fig. 5. In fact, the values of the residual dipolar coupling for the stem-bulge-stem region are similar between the kissing-loop and extended-duplex dimers (to be published). A preliminary normal mode analysis suggested the existence of hinge motion, and, in order to reveal the dynamic properties of the dimers, a molecular dynamics analysis, as well as the thermodynamics analysis (*33*), is required. The most obvious local difference was observed for A16; for the kissing-loop dimer, A16 was close to the same residue in the other molecule (Fig. 6A, left) and did not stack above A15 of the same molecule nor G17 of the other molecule (Fig. 6A, right), whereas for the extended-duplex dimer, A16 was apart from the same residue of the other molecule (Fig. 6B, left) and stacked between A15 and G17 (Fig. 6B, right).

Structural Comparison with Related Structures—Ennifar *et al.* (*20*) determined the crystal structure of

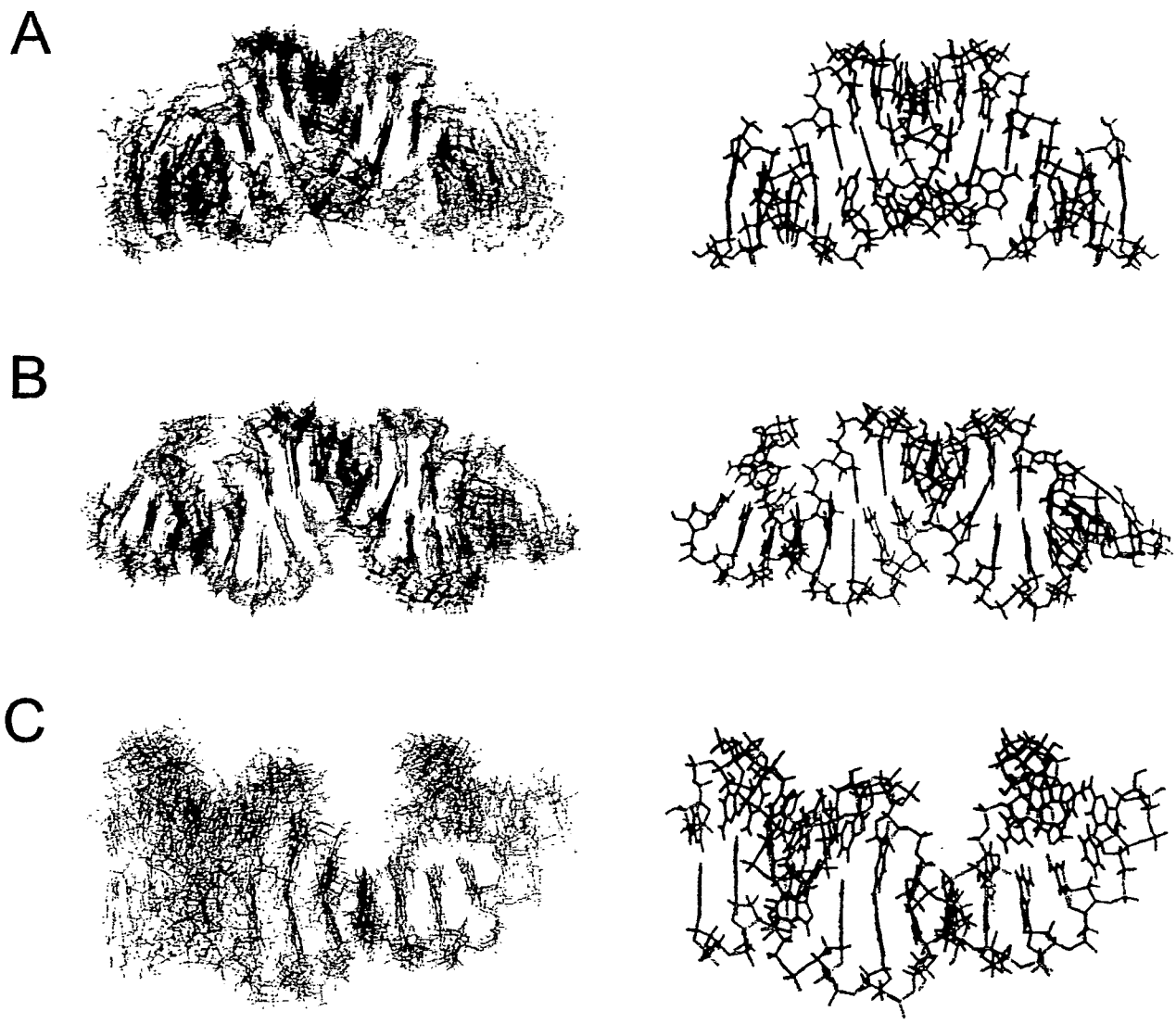

Fig. 4. **Solution structures of each part of DIS39.** Left panels show the superimposition of the 10 lowest energy structures and the right panels show the minimized average structures. (A) The loop region of loop25, as shown by the broken box in Fig. 1b, in the kissing-loop dimer. Each strand is colored in red or blue. (B) The loop region of loop25 in the extended-duplex dimer. (C) The stem-bulge-stem region of bulge34.

the kissing-loop dimer. The present structure is similar to the crystal structures in general, except for A15 and A16. In the present structure, A15 stacks on G14 and A16 interacts with the same residue in the other molecule (Fig. 6A, right). On the other hand, in the crystal structure, A15 and G16 are flipped out (*20*). It is noted that the numbering system of DIS39 is used for other structures for convenience, and position 16 is occupied by A or G depending on the strain. A15 and A16 (or G16) might be flexible and can be flipped out even in solution. Mujeeb *et al.* (*19*) determined the solution structure of the kissing-loop dimer. In this structure, A16 interacts with A15 and C24 in the other molecule, and, as a result, the distance between the two stems is relatively short. Thus, this restricted interaction makes the global structure different from the present structure and the crystal structure. However, the location of A15 is similar in the two solution structures. The difference in the conformation of A16 between the two solution structures may reflect the difference in the sequence of the stem adjacent to the loop and/or in the sample condition, including the salt concentration. The NOE connectivity determined in the present study agrees in general with those of Dardel *et al.* who analyzed the structure of the stem-loop region in the kissing-loop dimer by NMR (*34*).

Girard *et al.* (*21*) and Mujeeb *et al.* (*22*) determined the solution structures of extended-duplex dimers. In these two structures, as well as in the present structure, A15, A16 and A23 form a zipper like structure (Fig. 6B, right). On the other hand, in the case of the crystal structure of the extended-duplex dimer, G16 forms a G:A base pair and A15 is flipped out, and it was assumed that this in-out bulge transconformation is magnesium-dependent (*23*).

Structures of the stem-bulge-stem region were shown by Lawrence *et al.* (*26*) and Yuan *et al.* (*27*). In the solution structure determined by Lawrence *et al.* (*26*), continuous stackings were formed for each strand, G6-C8 and

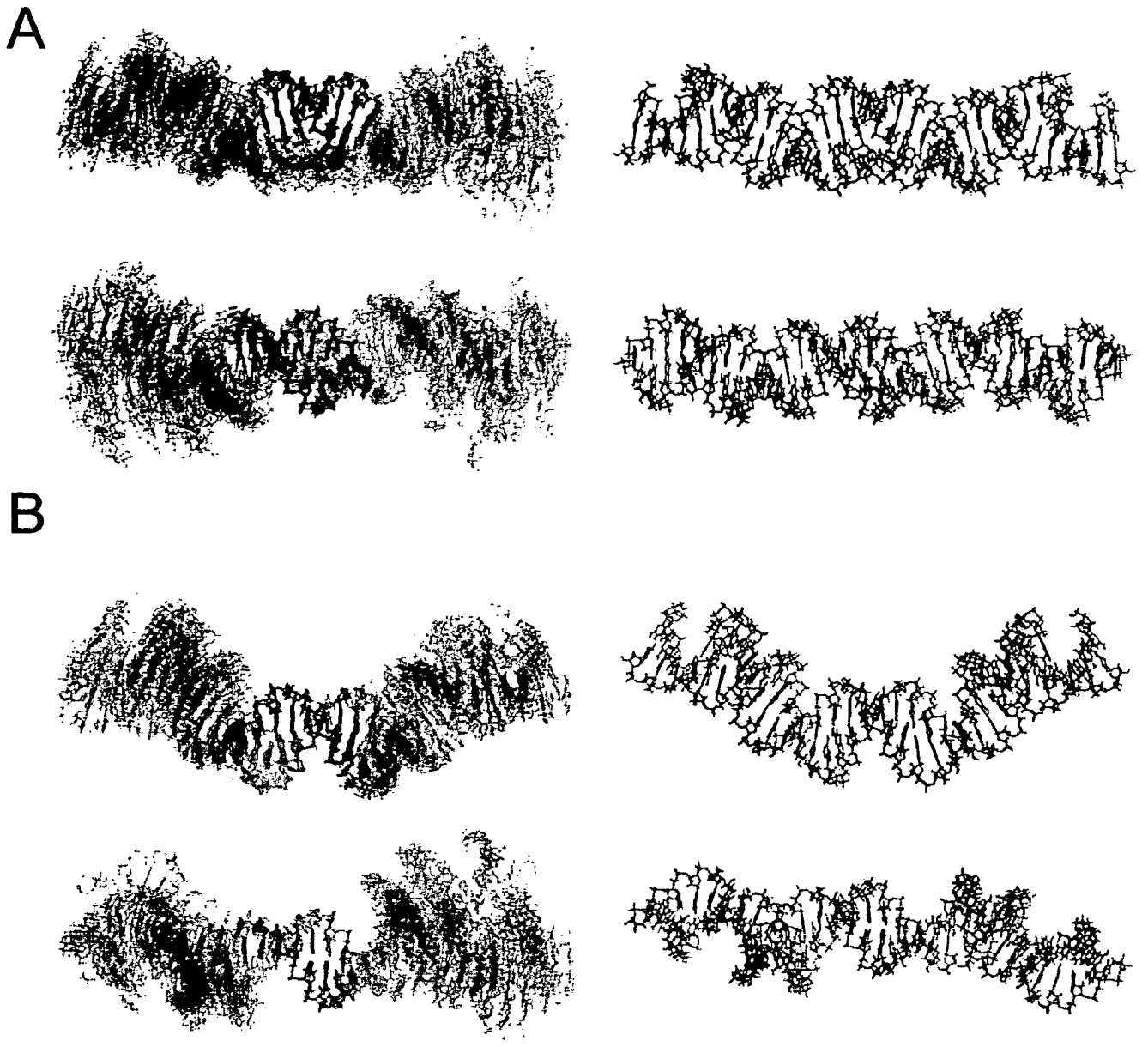

Fig. 5. **Solution structures of the (A) kissing-loop and (B) extended-duplex dimers of DIS39.** Left panels show the structures constructed by combining the structures of the loop (the 10 lowest energy structures of the kissing-loop or extended-duplex dimers) and the stem-bulge-stem (minimized average structure) regions. Right panels show the structures constructed by combining the minimized average structures of the loop and stem-bulge-stem regions. The two regions were combined by superimposing two base pairs, C12–G26 and U13–G25 (Fig. 1, gray area). Each strand is colored in red or blue and views from two different directions are shown.

G30-C34. Yuan *et al.* (*27*) showed that G7 and A31 form a base pair, and that G33 is not always stacked on G32 or C34, and, in general, the present structure is identical to the latter structure. Greatorex *et al.* (*25*) showed that the bulge region is too flexible to determine the conformation. These conformational differences may be caused by differences in the stability of the terminal stem. Lawrence *et al.* (*26*) adopted a stable 7 base-pair stem, and their structure forms an ordered conformation in the bulge region. In contrast, Greatorex *et al.* (*25*) adopted an unstable 4 base-pair stem and the bulge region is flexible. Yuan *et al.* (*27*) adopted a 4 base-pair stem and a flanking adenosine residue at the 3′ terminal that must stabilize the stem. In the present study, a 6 base-pair stem was used.

Mechanism of the Two Stem Dimerization—Between the kissing-loop and extended-duplex dimers, A16 shows the most drastic change in interaction with other residues, suggesting that A16 is the key residue in the two step dimerization reaction. The difference in the A16 conformation among structures with different sequences and determined under different conditions as described above, also suggests the importance of this residue. Mujeeb *et al.* (*19, 22*) also pointed out the flexibility around the junction of the loop and the stem of DIS in the kissing-loop and

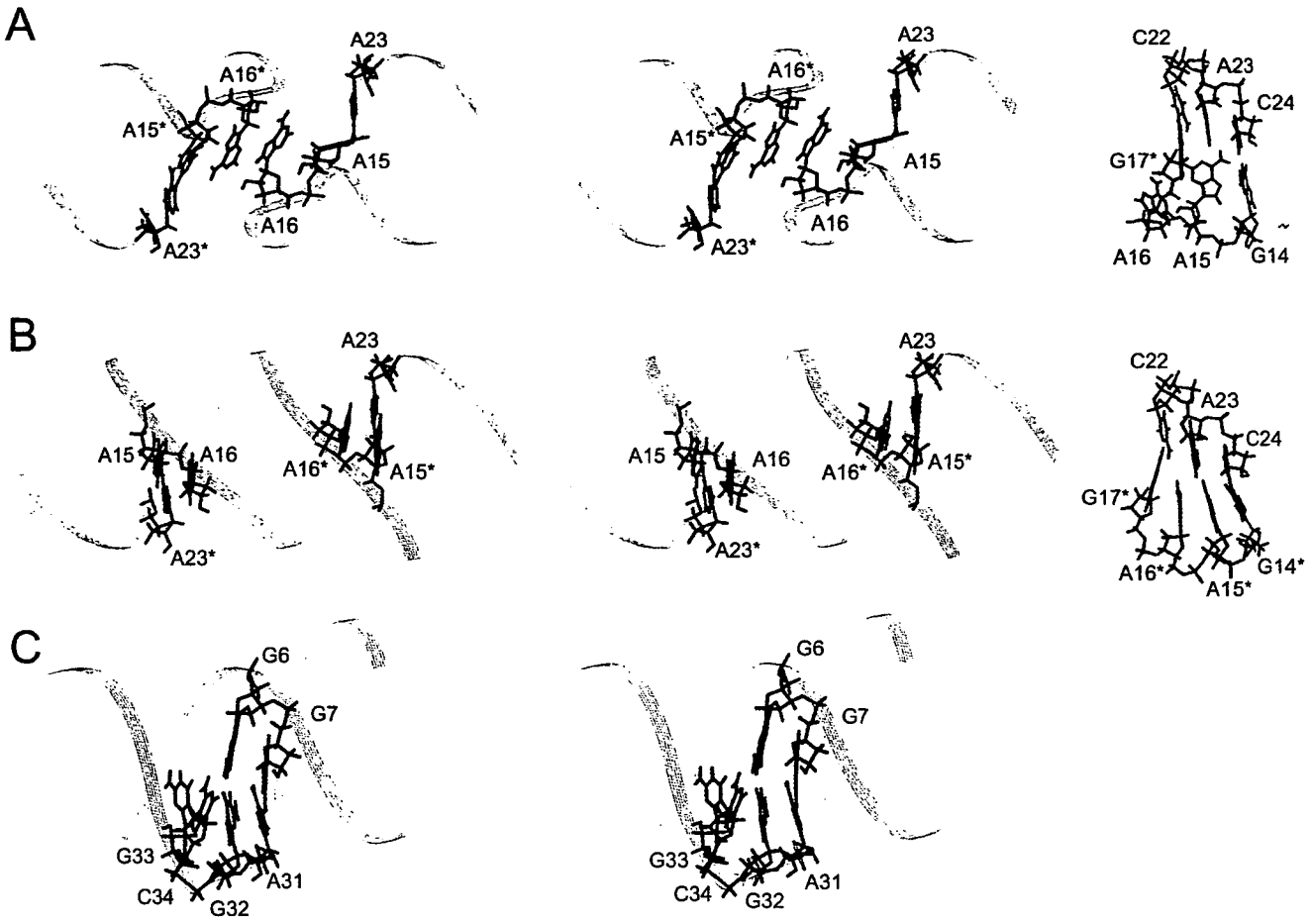

Fig. 6. **Structures of the linking regions.** (A) Regions linking the stem and loop in the kissing-loop dimer. The left panels show the positions of A15, A16, and A23 in the entire structure in a stereo view, and the right panels show residues linking the stem and loop. Asterisks indicate residues in the other strand. (B) Regions linking the stem and loop in the extended-duplex dimer. (C) The bulge region linking the two stems.

extended-duplex dimers. Imino proton signals due to U9:A29 and U10:A28 are much broader than other signals in the stem region, and no imino proton signal due to C8:G30 was observed. Thus, the stem between the loop and bulge is destabilized by the bulge region. Our previous experiments also showed that the bulge region is required for the two-step dimerization to adjust the thermal stability of DIS, and Greatorex *et al.* (*25*) also indicated that the flexibility of the bulge region is critical based on the fact that mutations in the bulge region strongly affect the melting temperature, as well as the fact that none of the wild-type sequences in the bulge region that increase the melting temperature is ever found in wild-type viruses. Thus, the conformational conversion from the kissing-loop dimer to the extended-duplex dimer might require two factors, the movement of A16 and the modest stability of the stem caused by the presence of the bulge region.

In the present study, a set of structures corresponding to the initial and final structures of the two-step dimerization of DIS are provided; these structures will promote studies to elucidate the molecular mechanism of the conformational change in the two-step dimerization, including an analysis of the interaction between DIS and NCp7, in addition to the molecular dynamics approach.

Coordinates: The structure has been deposited in the Protein Data Bank (accession code 2D17: the stem-bulge-stem region of bulge34, 2D18: the extended-duplex dimer of loop25, 2D19: the kissing-loop dimer of loop25, 2D1A: the extended-duplex dimer of DIS39 and 2D1B: the kissing-loop dimer of DIS39).

This work was supported by the "Research for the Future" Program (JSPS-RFTF97L00503) from the Japan Society for the Promotion of Science, and, in part, by a Grant-in-Aid for High Technology Research from the Ministry of Education, Science, Sports and Culture, Japan.

REFERENCES

1. Hoglund, S., Ohagen, A., Goncalves, J., Panganiban, A.T., and Gabuzda, D. (1997) Ultrastructure of HIV-1 genomic RNA. *Virology* **233**, 271–279
2. Laughrea, M., Jette, L., Mak, J., Kleiman, L., Liang, C., and Wainberg, M.A. (1997) Mutations in the kissing-loop hairpin of human immunodeficiency virus type 1 reduce viral infectivity as well as genomic RNA packaging and dimerization. *J. Virol.* **71**, 3397–3406
3. Clever, J.L. and Parslow, T.G. (1997) Mutant human immunodeficiency virus type 1 genomes with defects

in RNA dimerization or encapsidation. *J. Virol.* **71**, 3407–3414
4. Paillart, J.C., Berthoux, L., Ottmann, M., Darlix, J.L., Marquet, R., Ehresmann, B., and Ehresmann, C. (1996) A dual role of the putative RNA dimerization initiation site of human immunodeficiency virus type 1 in genomic RNA packaging and proviral DNA synthesis. *J. Virol.* **70**, 8348–8354
5. Laughrea, M. and Jette, L. (1994) A 19-nucleotide sequence upstream of the 5′ major splice donor is part of the dimerization domain of human immunodeficiency virus 1 genomic RNA. *Biochemistry* **33**, 13464–13474
6. Skripkin, E., Paillart, J.C., Marquet, R., Ehresmann, B., and Ehresmann, C. (1994) Identification of the primary site of the human immunodeficiency virus type 1 RNA dimerization *in vitro*. *Proc. Natl. Acad. Sci. USA* **91**, 4945–4949
7. Fu, W. and Rein, A. (1993) Maturation of dimeric viral RNA of Moloney murine leukemia virus. *J. Virol.* **67**, 5443–5449
8. Fu, W., Gorelick, R.J., and Rein, A. (1994) Characterization of human immunodeficiency virus type 1 dimeric RNA from wild-type and protease-defective virions. *J. Virol.* **68**, 5013–5018
9. Laughrea, M. and Jette, L. (1996) Kissing-loop model of HIV-1 genome dimerization: HIV-1 RNAs can assume alternative dimeric forms, and all sequences upstream or downstream of hairpin 248–271 are dispensable for dimer formation. *Biochemistry* **35**, 1589–1598
10. Muriaux, D., Fosse, P., and Paoletti, J. (1996) A kissing complex together with a stable dimer is involved in the HIV- 1Lai RNA dimerization process *in vitro*. *Biochemistry* **35**, 5075–5082
11. Muriaux, D., Girard, P.M., Bonnet-Mathoniere, B., and Paoletti, J. (1995) Dimerization of HIV-1Lai RNA at low ionic strength. An autocomplementary sequence in the 5′ leader region is evidenced by an antisense oligonucleotide. *J. Biol. Chem.* **270**, 8209–8216
12. Laughrea, M., Shen, N., Jette, L., Darlix, J., Kleiman, L., and Wainberg, M.A. (2001) Role of distal zinc finger of nucleocapsid protein in genomic RNA dimerization of human immunodeficiency virus type 1; No role for the palindrome crowning the R-U5 hairpin. *Virology* **281**, 109–116
13. de Guzman, R.N., Wu, Z.R., Stalling, C.C., Pappalardo, L., Borer, P.N., and Summers, M.F. (1998) Structure of the HIV-1 nucleocapsid protein bound to the SL3 ψ–RNA recognition element. *Science* **279**, 384–388
14. Amarasinghe, G.K., de Guzman, R.N., Turner, B.G., Chancellor, K.J., Wu, Z.R., and Summers, M.F. (2000) NMR structure of the HIV-1 nucleocapsid protein bound to Stem-Loop SL2 of the ψ–RNA packaging signal. Implications for Genome recognition. *J. Mol. Biol.* **301**, 491–511
15. Berkowitz, R., Fisher, J., and Goff, S.P. (1996) RNA packaging. *Curr. Top. Microbiol. Immunol.* **214**, 177–218
16. Darlix, J.L., Lopez-Lastra, M., Mély, Y., and Roques, B. (2003) Nucleocapsid protein chaperoning of nucleic acids at the heart of HIV structure, assembly and cDNA synthesis. In *HIV Sequence Compendium 2002* (Kuiken, C., Foley, B., Freed, E., Hahn, B., Marx, P., McCutchan, F., Mellors, J.W., Wolinsky, S., and Korber, B., eds.) pp. 69–88, Los Alamos National Laboratory, Los Alamos, NM
17. Takahashi, K., Baba, S., Koyanagi, Y., Yamamoto, N., Takaku, H., and Kawai, G. (2001) Two basic regions of NCp7 are sufficient for conformational conversion of HIV-1 dimerization initiation site from kissing-loop dimer to extended-duplex dimer. *J. Biol. Chem.* **276**, 31274–31278
18. Baba, S., Takahashi, K., Koyanagi, Y., Yamamoto, N., Takaku, H., Gorelick, R.J., and Kawai, G. (2003) Role of the Zinc Fingers of HIV-1 Nucleocapsid Protein in Maturation of Genomic RNA. *J. Biochem.* **134**, 637–639
19. Mujeeb, A., Clever, J.L., Billeci, T.M., James, T.L., and Parslow, T.G. (1998) Structure of the dimer initiation complex of HIV-1 genomic RNA. *Nat. Struct. Biol.* **5**, 432–436
20. Ennifar, E., Walter, P., Ehresmann, B., Ehresmann, C., and Dumas, P. (2001) Crystal Structures of Coaxially-Stacked Kissing Complexes of the HIV-1 RNA Dimerization Initiation Site. *Nat. Struct. Biol.* **8**, 1064–1068
21. Girard, F., Barbault, F., Gouyette, C., Huynh-Dinh, T., Paoletti, J., and Lancelot, G. (1999) Dimer Initiation Sequence of HIV-1Lai Genomic RNA: NMR Solution Structure of the Extended Duplex. *J. Biomol. Struct. Dyn.* **16**, 1145–1157
22. Mujeeb, A., Parslow, T.G., Zarrinpar, A., Das, C., and James, T.L. (1999) NMR structure of the mature dimer initiation complex of HIV-1 genomic RNA. *FEBS Lett.* **458**, 387–392
23. Ennifar, E., Yusupov, M., Walter, P., Marquet, R., Ehresmann, B., Ehresmann, C., and Dumas, P. (1999) The crystal structure of the dimerization initiation site of genomic HIV-1 RNA reveals an extended duplex with two adenine bulges. *Structure Fold Des.* **7**, 1439–1449
24. Ennifar, E., Walter, P., and Dumas, P. (2003) A Crystallographic Study of the Binding of 13 Metal Ions to Two Related RNA Duplexes. *Nucleic Acids Res.* **31**, 2671–2682
25. Greatorex, J., Gallego, J., Varani, G., and Lever, A. (2002) Structure and Stability of Wild-Type and Mutant RNA Internal Loops from the SL-1 Domain of the HIV-1 Packaging Signal. *J.Mol.Biol.* **322**, 543–557
26. Lawrence, D.C., Stover, C.C., Noznitsky, J., Wu, Z., and Summers, M. F. (2003) Structure of the Intact Stem and Bulge of HIV-1 Psi-RNA Stem-Loop Sl1. *J. Mol. Biol.* **326**, 529–542
27. Yuan, Y., Kerwood, D.J., Paoletti, A.C., Shubsda, M.F., and Borer, P.N. (2003) Stem of SL1 RNA in HIV-1: structure and nucleocapsid protein binding for a 1 × 3 internal loop. *Biochemistry* **42**, 5259–5269
28. Shen, N., Jette, L., Liang, C., Wainberg, M.A., and Laughrea, M. (2000) Impact of human immunodeficiency virus type 1 RNA dimerization on viral infectivity and of stem-loop B on RNA dimerization and reverse transcription and dissociation of dimerization from packaging. *J. Virol.* **74**, 5729–5735
29. Takahashi, K.I., Baba, S., Chattopadhyay, P., Koyanagi, Y., Yamamoto, N., Takaku, H., and Kawai, G. (2000) Structural requirement for the two-step dimerization of human immunodeficiency virus type 1 genome. *RNA* **6**, 96–102
30. Varani, G., Aboul-era, F., and Allain, F.H.-T. (1996) NMR investigation of RNA structure. *Prog. NMR Spect.* **29**, 51–127
31. Takahashi, K., Baba, S., Hayashi, S., Koyanagi, Y., Yamamoto, N., Takaku, H., and Kawai, G. (2000) NMR analysis on intra- and inter-molecular stems in the dimerization initiation site of the HIV-1 genome. *J. Biochem.* **127**, 681–639
32. St.Louis, D.C., Gotte, D., Sanders-Buell, E., Ritchey, D.W., Salminen, M.O., Carr, J.K., and McCutchan, F.E. (1998) Infectious molecular clones with the nonhomologous dimer initiation sequences found in different subtypes of human immunodeficiency virus type 1 can recombine and initiate a spreading infection in vitro. *J. Virol.* **72**, 3991–3998
33. Weixlbaumer, A., Werner, A., Flamm, C., Westhof, E., and Schroeder, R. (2004) Determination of thermodynamic parameters for HIV DIS type loop-loop kissing complexes. *Nucleic Acids Res.* **32**, 5126–5133
34. Dardel, R., Marguet, R., Ehresmann, C., Ehresmann, B., and Blanquet, S. (1998) Solution studies of the dimerization initiation site of HIV-1 genomic RNA. *Nucleic Acids Res.* **26**, 3567–3571

THE JOURNAL OF BIOLOGICAL CHEMISTRY
Vol. 280, No. 33, Issue of August 19, pp. 29409–29419, 2005
Printed in U.S.A.

Ras-ERK MAPK Cascade Regulates GATA3 Stability and Th2 Differentiation through Ubiquitin-Proteasome Pathway*[S]

Received for publication, March 2, 2005, and in revised form, June 3, 2005
Published, JBC Papers in Press, June 23, 2005, DOI 10.1074/jbc.M502333200

Masakatsu Yamashita‡, Ryo Shinnakasu‡, Hikari Asou‡, Motoko Kimura‡, Akihiro Hasegawa‡, Kahoko Hashimoto§, Naoya Hatano¶, Masato Ogata¶, and Toshinori Nakayama‡‖

From the ‡Department of Immunology, Graduate School of Medicine, Chiba University, 1-8-1 Inohana Chuo-ku, Chiba 260-8670, the §Department of Life and Environmental Sciences and High Technology Research Center, Chiba Institute of Technology, Narashino, Tsudanuma, Chiba 275-0016, and the ¶Department of Biochemistry, Mie University School of Medicine, 2-174, Edobashi, Tsu, Mie 514-8507, Japan

Differentiation of naive CD4 T cells into Th2 cells requires protein expression of GATA3. Interleukin-4 induces STAT6 activation and subsequent GATA3 transcription. Little is known, however, on how T cell receptor-mediated signaling regulates GATA3 and Th2 cell differentiation. Here we demonstrated that T cell receptor-mediated activation of the Ras-ERK MAPK cascade stabilizes GATA3 protein in developing Th2 cells through the inhibition of the ubiquitin-proteasome pathway. Mdm2 was associated with GATA3 and induced ubiquitination on GATA3, suggesting its role as a ubiquitin-protein isopeptide ligase for GATA3 ubiquitination. Thus, the Ras-ERK MAPK cascade controls GATA3 protein stability by a post-transcriptional mechanism and facilitates GATA3-mediated chromatin remodeling at Th2 cytokine gene loci leading to successful Th2 cell differentiation.

In peripheral lymphoid organs, naive CD4 T cells that have recognized specific antigens differentiate into either one of two distinct helper T cell subsets, Th1 and Th2 cells (1). Upon antigen restimulation, Th1 cells produce large amounts of IFNγ[1] and direct cell-mediated immunity against intracellular pathogens. Th2 cells produce IL-4, IL-5, and IL-13 and are involved in humoral immunity and allergic reactions. The direction of Th cell differentiation depends on the types of cytokine in the environmental milieu (2, 3). Naive CD4 T cells stimulated with antigens in the presence of IL-12 differentiate into Th1 cells, whereas the presence of IL-4 drives differentiation into Th2 cells (4–6). IL-12-mediated activation of signal transducer and activator of transcription (STAT) 4 is crucial for Th1 cell differentiation, and IL-4-mediated STAT6 activation is important for Th2 cell development (7–9).

In addition to the cytokines mentioned above, activation of TCR-mediated signaling is also indispensable for both Th1 and Th2 cell differentiation. We reported that Th2 cell differentiation is highly dependent on the extent of TCR-mediated activation of the p56^{lck}, calcineurin, and Ras-ERK MAPK signaling cascade (10–12). In particular, inhibition of the activation of the Ras-ERK MAPK cascade caused a shift from Th2 to Th1 cell differentiation, suggesting that the direction of Th1/Th2 cell differentiation could be controlled by TCR-mediated activation of the Ras-ERK MAPK cascade (11, 13). On the other hand, Th1 cell development appeared to be regulated by another MAPK, c-Jun N-terminal kinase (14, 15).

Recently, several transcription factors that control Th1/Th2 cell differentiation were identified (8, 16). Among them, GATA3 appears to be a key factor for Th2 cell differentiation. GATA3 is selectively induced in developing Th2 cells after TCR stimulation in the presence of IL-4, and ectopic expression of GATA3 resulted in the induction of Th2 cell differentiation in the absence of STAT6 (17–20). GATA3 was found to be important for the maintenance of the Th2 phenotype (21, 22).

Th2 cell differentiation is accompanied by chromatin remodeling of the Th2 cytokine (IL-4/IL-5/IL-13) gene loci, *e.g.* hyperacetylation of histones H3 and H4 (23–25). Hyperacetylation of the IL-4 and IL-13 gene loci (23) and that of IL-5 gene locus (26) are highly dependent on the expression of GATA3. We described a precise map of the Th2-specific histone hyperacetylation within the Th2 cytokine gene loci, and we identified a 71-bp conserved GATA3-response element at 1.6 kbp upstream of the IL-13 locus (23). The GATA3-response element appears to play a crucial role for GATA3-mediated targeting and downstream spreading of core histone hyperacetylation within the IL-13 and IL-4 gene loci in developing CD4$^+$ Th2 and CD8$^+$ Tc2 cells (23, 27).

One of the major pathways of degradation of short lived regulatory proteins, including transcriptional factors, is through ubiquitin-mediated targeting and protein destruction in the 26 S proteasome. Protein ubiquitination is involved in a wide range of cellular processes, including cell cycle progression, signal transduction, transcriptional regulation, DNA re-

* This work was supported by grants from the Ministry of Education, Culture, Sports, Science and Technology (Japan), Grants-in-aid for Scientific Research Priority Areas Research 13218016 and 16043211, Scientific Research B 14370107, Scientific Research C 16616003 and 15790248, and Special Coordination Funds for Promoting Science and Technology, the Ministry of Health, Labor, and Welfare (Japan), the Program for Promotion of Fundamental Studies in Health Science of the Organization for Pharmaceutical Safety and Research (Japan), The Japan Health Science Foundation, Uehara Memorial Foundation, and Mochida Foundation. The costs of publication of this article were defrayed in part by the payment of page charges. This article must therefore be hereby marked "*advertisement*" in accordance with 18 U.S.C. Section 1734 solely to indicate this fact.

[S] The on-line version of this article (available at http://www.jbc.org) contains Fig. 1.

‖ To whom correspondence should be addressed: Dept. of Immunology (H3), Graduate School of Medicine, Chiba University, 1-8-1 Inohana, Chuo-ku, Chiba, 260-8670 Japan. Tel.: 81-43-226-2200; Fax: 81-43-227-1498; E-mail: tnakayama@faculty.chiba-u.jp.

[1] The abbreviations used are: IFNγ, interferon-γ; dn, dominant-negative; ERK, extracellular signal-regulated kinase; Erk2 sem., an active form of ERK2; KO, knock out (deficient); Tg, transgenic; Ub, ubiquitination; WT, wild type; TCR, T cell receptor; STAT, signal transducer and activator of transcription; IL, interleukin; PMA, phorbol 12-myristate 13-acetate; mAb, monoclonal antibody; ChIP, chromatin immunoprecipitation; MAPK, mitogen-activated protein kinase; MEK, MAPK/ERK kinase; siRNA, small interfering RNA; CHX, cycloheximide; GFP, green fluorescent protein; EGFP, enhanced GFP; hNGFR, human nerve growth factor receptor p75; FCS, fetal calf serum; E3, ubiquitin-protein isopeptide ligase.

pair, antigen presentation, and apoptosis (28–31). Emerging views suggest that various aspects of the immune system are controlled by ubiquitination (32). A well known example of the ubiquitin-dependent regulation in the immune system is the proteasome-dependent processing of peptides in antigen-presenting cells (33). It is also well known that lipopolysaccharide or proinflammatory cytokines such as IL-1 can induce activation of NF-κB through ubiquitination and subsequent degradation of the inhibitor of κB (34). However, a role for the ubiquitin-mediated regulation of Th1/Th2 cell differentiation has not been reported.

In the present study, we investigated the molecular targets of the Ras-ERK MAPK cascade that control chromatin remodeling of the Th2 cytokine gene loci and subsequent Th2 cell differentiation, and we found that the Ras-ERK MAPK cascade controls the stability of the GATA3 protein through the ubiquitin-proteasome pathway. Moreover, we demonstrated that the ubiquitination of GATA3 by Mdm2 is dependent on a ring finger domain.

EXPERIMENTAL PROCEDURES

Mice—C57BL/6 mice were purchased from SLC (Shizuoka, Japan). STAT6-deficient (KO) mice were kindly provided by Shizuo Akira (Osaka University, Osaka, Japan) (35). A T cell-specific H-ras dominant-negative (dnRas) transgenic (Tg) mouse with the *lck* proximal promoter was described elsewhere (11, 36). All mice used in this study were maintained under specific pathogen-free conditions.

Reagents—PD98059 (Calbiochem), cycloheximide (Calbiochem), MG132 (Sigma), and U0126 (Promega) were purchased.

Expression Plasmids and Transfection—Myc-tagged and FLAG-tagged GATA3 mutants (pCMV Tag 3B-GATA3 WT, dCT, dCF, and dZF), and GFP-fused GATA3 mutants (pEGFP-C1 GATA3 WT and pEGFP-C1 GATA3 dZF) were generated by PCR-based mutation. Myc-tagged wild type Mdm2, RING finger-deleted Mdm2 (pCMV Tag-3B-Mdm2 WT, dR), and $p19^{ARF}$ were generated in our laboratory. COS, 293T, and NIH3T3 cells were transfected using FuGENE reagent (Invitrogen) according to the manufacturer's protocol.

Cell Cultures and in Vitro T Cell Differentiation—CD4 T cells were purified using magnetic beads and an auto-MACS® sorter (Miltenyi Biotec), yielding a purity of >98%. The purified CD4 T cells (1.5×10^6) were stimulated for 2 days with immobilized anti-TCR mAb (H57–597, 3 μg/ml) in the presence of IL-2 (25 units/ml), IL-12 (100 units/ml), and anti-IL-4 mAb (11B11, 25% culture supernatant) for Th1-conditions or in the presence of IL-2 (25 units/ml), IL-4 (100 units/ml), and anti-IFNγ mAb (R4.6A2, 25% culture supernatant) for Th2− conditions. The cells were cultured for another 3 days in the presence of only the cytokines present in the initial culture. The numbers of Th1/Th2 cells were determined by using intracellular staining with anti-IL-4 and anti-IFNγ as described (10).

Retroviral Vectors and Infection—pMX-IRES-CAR (human coxsackie-adenovirus receptor) plasmid was generated from the pMX-IRES-GFP plasmid by replacing the EGFP gene with the CAR gene. The methods for the generation of virus supernatant and the infection were described previously (37). Infected cells were subjected to intracellular staining with anti-IL-4 and anti-IFNγ mAb or to cell sorting. To prepare large numbers of infected cells for immunoblotting, the pMX-IRES-CAR or pMXs-IRES-hNGFR vector was used, and the infected cells were enriched by auto-MACS® sorter with anti-CAR mAb (38) or anti-human NGFR (C40–1457; Pharmingen). cDNA encoding Erk2 sem was described previously (39). pMXs-Mdm2 dR-hNGFR was constructed by inserting Mdm2-dR into a multicloning site of pMXs-IRES-hNGFR. cDNA for human GATA3 or an active form of human Raf-1 (40) was inserted into a multicloning site of pMX-IRES-GFP.

Chromatin Immunoprecipitation (ChIP) Assay—ChIP was performed using the histone H3 assay kit (catalog number 17-245; Upstate Biotechnology, Inc.) as described previously (23). Semi-quantitative PCR was performed with DNA samples from 3 or 1×10^4 cells at 28 cycles. PCR products were resolved in an agarose gel and visualized by ethidium bromide. Images were recorded and quantified using ATTO L & S analyzer (ATTO, Tokyo, Japan). The primers used were described previously (23).

Immunoprecipitation and Immunoblotting—Purified CD4 T cells were stimulated with immobilized anti-TCR mAb for 2 days as described above, and nuclear extracts were prepared with an NE-PER™ nuclear and cytoplasmic extract reagent (catalog number 78833; Pierce) according to the manufacturer's protocol. The amount of GATA3, c-Maf, or α-tubulin was assessed by immunoblotting with anti-GATA3 mouse mAb (HG3–31; Santa Cruz Biotechnology, Santa Cruz, CA), anti-c-Maf rabbit antisera (M-153; Santa Cruz Biotechnology), or anti-α-tubulin mAb (DM1A; Lab Vision Corp.) as described previously (37). Anti-Mdm2 mAb (D-17; Santa Cruz Biotechnology), anti-E6-AP mAb (clone 20; BD Transduction Laboratories), anti-Itch mAb (clone 32; BD Transduction Laboratories), and anti-Cbl-b mAb (G-1; Santa Cruz Biotechnology) were used for immunoblotting. For transfectants, anti-FLAG mAb (M2; Sigma) and anti-Myc mAb (PL14; MBL) were used for immunoblotting.

For anti-ubiquitin blotting, COS cells were transfected with Myc-tagged GATA3 vectors (pCMV Tag 3B). Two days later, cells were treated with cycloheximide (100 μM) and U0126 (20 μM) in the presence or absence of the proteasome inhibitor MG132 (50 μM) for 2 h. The cells were then pelleted, resuspended in RIPA buffer, and lysed on ice for 30 min. Insoluble material was removed by centrifugation. The lysates were incubated with 5 μg of anti-Myc mAb (MBL, Japan) for 2 h at 4 °C. 50 μl of protein G-conjugated Sepharose (Amersham Biosciences) was then added and incubated for an additional 1 h. After removal of the supernatant, the beads were washed twice with RIPA buffer. The bound protein was eluted by adding 25 μl of SDS sample buffer and was subjected to immunoblot analysis using mAb specific for ubiquitin (FK2; MBL, Tokyo, Japan).

Northern Blotting—Total RNA (20 μg) was isolated from cultured cells using TRIzol reagent (Invitrogen), separated on a 1% formaldehyde gel, and transferred to a Nytran Plus membrane (Schleicher & Schuell). Probes for GATA3 and β-actin were generated by PCR using the primers described previously (37). The digoxigenin labeling and detection system (Roche Diagnostics) was used for visualization.

Pulse-Chase Experiment—Splenic CD4 T cells were stimulated for 2 days under Th2− conditions. The cells were washed, preincubated for 30 min in methionine/cysteine-free medium, and pulsed for 30 min with 200 μCi/ml [^{35}S]methionine/cysteine (ICN). Then the cells were washed twice with Dulbecco's modified Eagle's medium containing nonradioactive 5 mM L-methionine, 3 mM L-cysteine, and 0.25% FCS, and chased in the same medium in the presence of PMA (3 ng/ml) or PMA plus U0126 (20 μM). U0126 was used in the pulse-chase experiment because it is known to inhibit preactivated MEK as well (41).

In Vitro Ubiquitination Assay—*In vitro* ubiquitination assay was performed as described previously (42). In brief, 293T cells were transfected with FLAG-tagged GATA3, and 3 days later the cells were treated with MG132 for 2 h. Then the cells were lysed in RIPA buffer (2.5×10^6 cells/ml), and the cell lysates (250 μl) were subjected to immunoprecipitation with anti-FLAG or anti-GATA3 mAb. The immunoprecipitates were incubated for 2 h at 30 °C in 25 μl of reaction buffer containing 50 mM Tris-HCl (pH 8.0), 50 ng of recombinant mouse ubiquitin-activating enzyme, 500 ng of ubiquitin carrier protein, 5 μg of glutathione *S*-transferase-Ub, 1 mM dithiothreitol, 2 mM $MgCl_2$, and 4 mM ATP. After terminating the reaction by the addition of 2× SDS sample buffer, immunoblotting with anti-GATA3 or anti-FLAG mAb was performed. Recombinant mouse ubiquitin-activating enzyme, ubiquitin carrier protein, and glutathione *S*-transferase-Ub were kindly provided by Dr. Keiji Tanaka (Tokyo Metropolitan Institute for Medical Science, Tokyo, Japan).

siRNA—Introduction of siRNA into a T cell line TG40 was performed as described (43). In brief, 2 μl of TransIT-TKO transfection reagent (Mirus) was diluted in 50 μl of serum-free/antibiotic-free RPMI 1640 per well. Ten minutes later, 1 μl of 40 μM siRNA was added to the diluted transfection reagent and incubated for 30 min with gentle agitation. Then the siRNA solution was added to TG40 cultures containing 5×10^5 cells in 500 μl of medium per well in a 24-well plate. Three days after transfection, ubiquitination of GATA3 and the expression of Mdm2 protein were assessed by immunoblotting. Pre-designed siRNA for Mdm2 was purchased from Ambion (16704), and control siRNA was from Santa Cruz Biotechnology (sc-37007).

RESULTS

The Ras-ERK MAPK Cascade Controls Histone Hyperacetylation of the Th2− Cytokine Gene Loci—We reported that Th2 cell differentiation and certain Th2 responses are dependent on the extent of activation of the Ras-ERK MAPK cascade (11, 13). Hyperacetylation of the Th2 cytokine gene loci was highly dependent on the expression of GATA3 (23, 26). We present here further confirmation of the observations in chromatin remodeling of the Th2 gene loci. The generation of IL-4-produc-

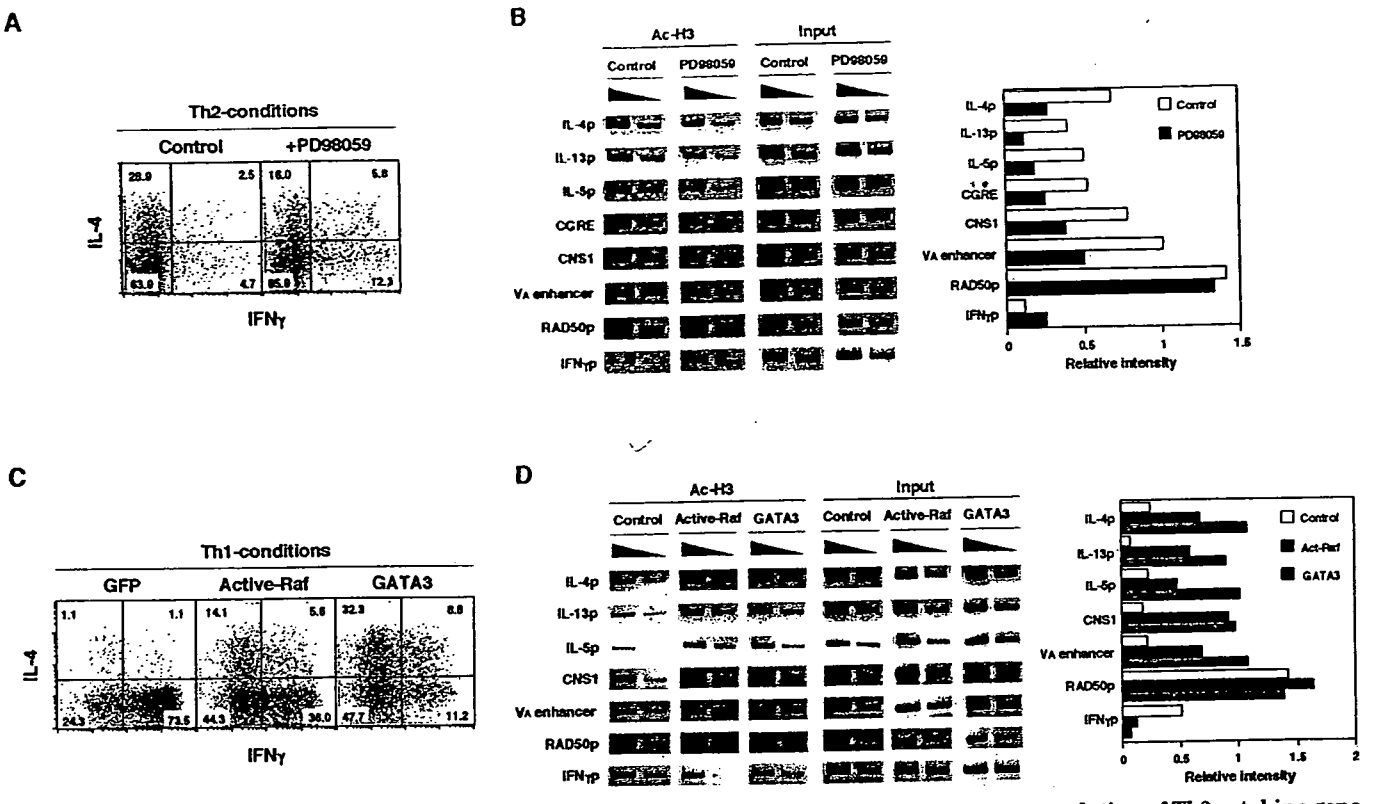

FIG. 1. **Activation of the ERK-MAPK cascade is required for GATA3-dependent histone H3 hyperacetylation of Th2 cytokine gene loci.** *A*, Th2 cell differentiation was inhibited by PD98059, a specific inhibitor of MEK. Freshly prepared splenic CD4 T cells were stimulated under Th2− conditions in the presence of PD98059 (30 μM) for 2 days. The cells were cultured for an additional 3 days and then stimulated with immobilized anti-TCR mAb. The numbers of Th1/Th2 cells were determined by intracellular staining with anti-IL-4 and anti-IFNγ. The *numbers* represent the percentages of cells in each quadrant. *B*, the effect of PD98059 on the histone H3 hyperacetylation. An aliquot of the cells cultured as in *A* were harvested on day 3, and the acetylation status of histone H3 in nucleosomes associated with the indicated regions was assessed by ChIP assay. An anti-acetylated histone H3 (K9, K14) antibody and specific primer pairs were used. Three independent experiments were performed, and similar results were obtained. Relative band intensities normalized by input DNA bands measured by a densitometer are shown in the *right panel*. *C*, expression of active Raf-induced IL-4 producing Th2 cells under Th1− conditions. Freshly prepared splenic CD4 T cells were stimulated under Th1− conditions and infected with retrovirus encoding active Raf or GATA3 bicistronically with EGFP on day 2. Three days later, the cells were stimulated with anti-TCR and were subjected to IL-4/IFNγ staining. *D*, histone H3 hyperacetylation on Th2 cytokine gene loci was induced by an active form of Raf-1 (*Active-Raf*) or ectopic expression of GATA3 in developing Th1 cells. GFP-positive infected CD4 T cells were enriched by cell sorting. *Control* represents mock vector virus infection. Acetylation status of histone H3 was determined by ChIP assay. Three independent experiments were done with similar results. Relative band intensities normalized by input DNA bands are shown in the *right panel*.

ing cells was substantially inhibited in the presence of a specific inhibitor of MEK (an ERK MAPKK), PD98059 (Fig. 1*A*). Fig. 1*B* shows that the acetylation levels of histones associated with the Th2 cytokine gene loci (IL-4 promoter, IL-13 promoter, IL-5 promoter, GATA3-response element, CNS1, and IL-4 V_A enhancer) were significantly reduced in the presence of PD98059. In the case of RAD50, there was no significant effect with PD98059 treatment, and with the IFNγ promoter (IFNγp) there was some enhancement in the acetylation. Under Th1 culture conditions, PD98059 exhibited no detectable inhibition of acetylation at the IFNγ promoter region (data not shown).

In addition, the effect of ectopic expression of an active form of Raf-1 (active-Raf) on the generation of Th1/Th2 cells was assessed. Significant numbers of IL-4-producing Th2 cells and a suppression of the generation of IFNγ-producing cells were observed in active Raf-infected cells stimulated under Th1− conditions (Fig. 1*C*). As a positive control, GATA3 infection was included, and in this case substantial levels of IL-4-producing cells with decreased numbers of IFNγ-producing cells were detected. Assessment of the acetylation status of histones in the active Raf-infected or GATA3-infected T cells defined by GFP expression on day 2 revealed significant increases in acetylation at the IL-4, IL-13, and IL-5 promoters and CNS1 and IL-4 V_A enhancer regions; however, the effect on the RAD50 promoter region was marginal (Fig. 1*D*). A significant decrease in the acetylation of the IFNγ promoter region was observed in the presence of active Raf. The levels of acetylation induced by active Raf infection were lower than those induced by GATA3. A possible explanation for this could be the limited expression of GATA3 in T cells cultured under Th1− conditions. Nevertheless, it is clear that the ERK-MAPK cascade controls GATA3-dependent histone hyperacetylation of the Th2 cytokine gene loci in developing Th2 cells.

Activation of the Ras-ERK MAPK Cascade Is Required for Stable Expression of GATA3 Protein in Developing Th2 Cells—GATA3 is a critical transcriptional factor for Th2 cell differentiation (17–19), and its expression is induced selectively under Th2− conditions. Here we demonstrate this in freshly prepared splenic CD4 T cells stimulated under Th1 and Th2 conditions (Fig. 2*A*, compare *lanes 1* and *3* and *lanes 2* and *4*). Treatment of Th2 condition cultures with PD98059 resulted in decreased protein expression of GATA3 (Fig. 2*A*, *lanes 5* and *6*). Similarly, the induction of GATA3 protein in dominant-negative Ras (dnRas) Tg T cells was significantly lower than that seen in the control, and this is consistent with the observation of impaired Th2 cell differentiation in dnRas Tg mice (11). A specific inhibitor for the p38 MAPK cascade (SB203580) did not affect the GATA3 expression in developing Th2 cells (data not shown). The activation of STAT6 is known to be critical for GATA3 transcription, and as expected, STAT6-deficient (STAT6 KO) CD4 T cells failed to induce GATA3 protein.

Concurrently, the transcriptional levels of GATA3 in T cells

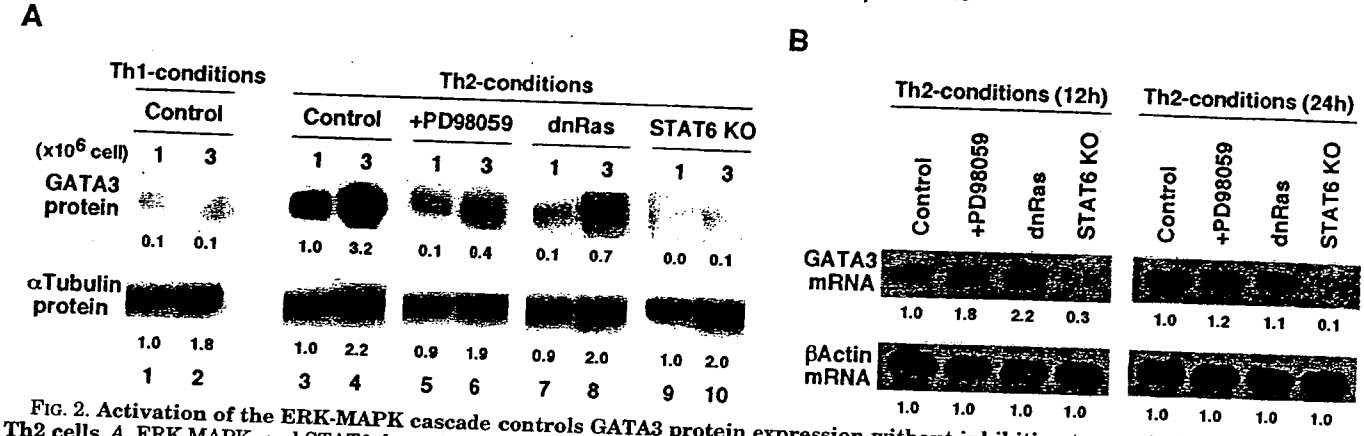

FIG. 2. **Activation of the ERK-MAPK cascade controls GATA3 protein expression without inhibiting transcription in developing Th2 cells.** *A*, ERK MAPK- and STAT6-dependent expression of GATA3 protein. Freshly prepared splenic CD4 T cells were stimulated under the indicated conditions for 2 days, and the expression of GATA3 protein in nuclei was assessed. CD4 T cells from T cell-specific dominant-negative H-Ras (dnRas) Tg mice and STAT6-deficient (STAT6 KO) mice were also used. The expression of α-tubulin was assessed as a control. A representative result from one of three independent experiments is shown. Arbitrary densitometric units normalized with α-tubulin bands are shown below each band. *B*, no effect of inhibition of the ERK-MAPK cascade on the transcriptional up-regulation of GATA3. Splenic CD4 T cells were stimulated under Th2− conditions for 12 and 24 h, and the expression levels of GATA3 mRNA were determined by Northern blot analysis. To examine the role for ERK-MAPK cascade activation, PD98059 (30 μM) and the CD4 T cells from dnRas Tg mice were used. Three independent experiments were performed with similar results. Arbitrary densitometric units are shown below each band.

cultured under Th2 conditions (12 and 24 h) as in Fig. 2*A* were assessed (Fig. 2*B*). The inhibition of activation of the Ras-ERK MAPK cascade by PD98059 or overexpression of dnRas transgene in T cells had no blocking effect on GATA3 mRNA expression. Rather, significant enhancement of GATA3 levels was detected at the 12-h time point. In contrast, GATA3 mRNA was not induced to significant levels in STAT6-deficient CD4 T cells, which is consistent with the lack of induced GATA3 protein.

Consequently, we sought to investigate further the consequence of the inhibition of ERK MAPK activation on the degradation of GATA3 protein. Splenic CD4 T cells were first stimulated under Th2− conditions for 2 days prior to being cultured without IL-4 or immobilized anti-TCR mAb for various time periods (chase) in either the presence or absence of another specific MEK inhibitor (U0126), which is also effective on activated MEK (Fig. 3, *A* and *B*). Under normal culture conditions with 10% FCS, the levels of GATA3 protein remained elevated over 12 h but then they declined significantly at 24 h. In the presence of U0126, significant reduction of GATA3 protein was observed at the 6- and 12-h time points, and the protein was virtually undetectable after a 24-h chase (Fig. 3*A*). U01126 treatment did not affect the level of another Th2-specific transcription factor, c-Maf. Under culture conditions with low levels of FCS (0.25%), where decreased levels of background stimulation of the MAPK cascades were detected (data not shown), a gradual decrease in GATA3 protein was seen and a modest rescue by the presence of PMA was observed (Fig. 3*B*). In the presence of U0126, the loss of GATA3 protein was dramatic, and GATA3 was barely detectable at the 12- and 24-h time points.

As an alternative means to assess the effect of ERK MAPK on the stability of the GATA3 protein, we performed pulse-chase experiments to follow the degradation of GATA3, and we found that the amount of ^{35}S-labeled nascent GATA3 protein was degraded very rapidly in the presence of U0126 (Fig. 3*C*). These results clearly demonstrate that rapid degradation of GATA3 occurs when activation of ERK MAPK is inhibited.

As a more direct test of the requirement for the activation of ERK MAPK to stabilize GATA3 in developing Th2 cells, we introduced an active form of ERK2 (Erk2 sem) (39) or a dominant-negative form of ERK2 (dnErk2) (44) into developing Th2 cells (Fig. 3*D*). As anticipated, GATA3 protein was significantly retained in cells infected with ERK2 sem, whereas the expression of dnERK2 significantly enhanced its degradation. Thus, the stability of GATA3 protein in developing Th2 cells appears to be highly dependent on the activation of the Ras-ERK MAPK cascade.

GATA3 Is Rapidly Degraded through the 26 S Proteasome Pathway—It would seem very likely that the proteasome pathway would be involved. To determine whether the 26 S proteasome is involved with the rapid degradation of the GATA3 protein, the effect of a proteasome inhibitor MG132 was examined. COS cells were transfected with Myc-tagged GATA3 and treated with cycloheximide (CHX) to inhibit protein synthesis in the presence or absence of MG132 for 1 or 2 h. Myc-tagged GATA3 was predominantly expressed in the nucleus, and after CHX treatment it was degraded rapidly in the absence of MG132 (Fig. 4*A*, *left panel*). In contrast, in the presence of MG132, there was a dramatic increase in the amount of Myc-tagged GATA3 protein in both nuclear and cytoplasmic fractions (Fig. 4*A*, *right panel*). Moreover, in developing Th2 cells GATA3 protein was degraded rapidly in the presence of CHX, and the degradation was inhibited by MG132 (Fig. 4*B*). In addition, another proteasome inhibitor lactacystin was tested in primary T cells for its ability to affect the degradation of GATA3, and a significant blocking of the degradation of GATA3 was observed (Fig. 4*C*). Collectively, these results point to the involvement of the 26 S proteasome pathway in the degradation of GATA3.

The C-terminal Region of GATA3 Including the Zinc Finger Domain Is Critical for Proteasome-dependent Degradation—In an attempt to map the target region of GATA3 that is critical for proteasome-dependent degradation, we prepared several truncated GATA3 mutants of the N-terminal region, which contains many lysine residues that can be ubiquitinated (Fig. 4*D*). Myc-tagged wild type (WT), dCT, dCF, and dZF constructs were transfected into COS cells, and the expression levels of GATA3 were assessed after treatment with MG132 (Fig. 4*E*). In comparison to wild type GATA3, there was essentially no difference in the pattern of disappearance of either the dCT or dCF mutant forms from nuclear fractions following CHX treatment, or in the retention of GATA3 protein by MG132 treatment. In the cytosol fraction of transfectants without drug treatment, slightly increased levels of protein were detected with dCT and dCF mutants, but the levels after treatment with MG132 were indistinguishable (Fig. 4*E*, *lower panels*). In sharp contrast, large amounts of dZF mutant protein were detected in

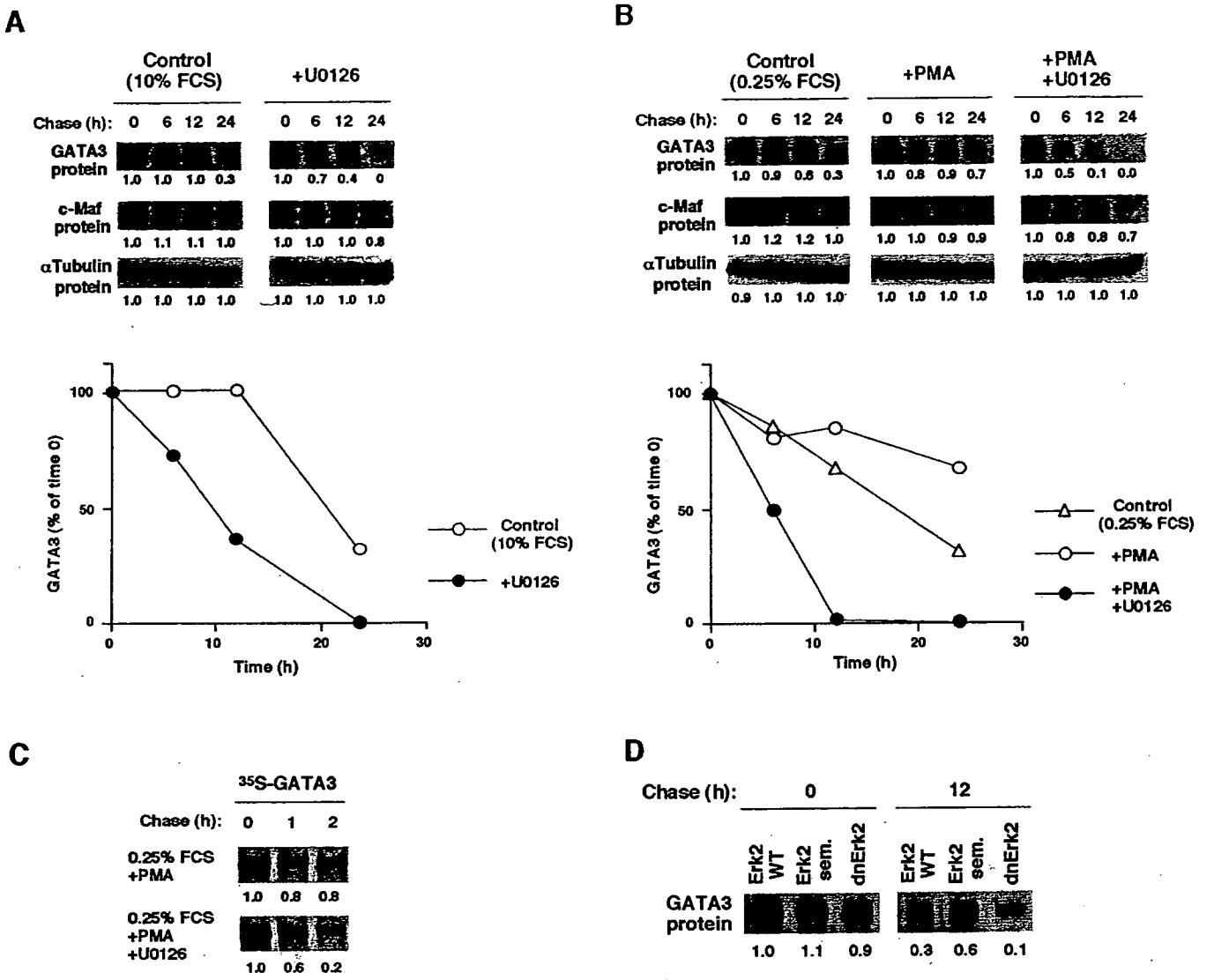

FIG. 3. **Regulation of the expression of GATA3 protein in developing Th2 cells by the ERK-MAPK cascade.** *A*, inhibition of ERK MAPK activation induces GATA3 protein degradation. Splenic CD4 T cells were stimulated under Th2− conditions for 2 days. The cells were then cultured for 6 and 12 h without cytokines in the presence or absence of MEK inhibitor U0126 (20 μM) with 10% FCS in the medium. The expression of GATA3 protein was assessed as in Fig. 2*A*. The expression of c-Maf and α-tubulin protein was also determined as controls. Arbitrary densitometric units are shown below each band, and the percentages of each point are shown in a *graph*. Three independent experiments with different time courses were performed with similar results. *B*, GATA3 protein degradation in the presence of PMA and U0126. Splenic CD4 T cells were stimulated for 2 days as described in *A*. Then the cells were cultured in the presence of PMA (3 ng/ml) and U0126 (20 μM) with just 0.25% FCS in the medium. The protein expression levels of GATA3, c-Maf, and α-tubulin protein were examined. Three independent experiments were performed, and a representative result is shown. *C*, degradation of GATA3 determined by pulse-chase analysis. Splenic CD4 T cells were stimulated as described in *A*. Then the cultured cells were labeled with [^{35}S]methionine and [^{35}S]cysteine and chased in a medium containing 0.25% FCS, nonradioactive methionine and cysteine in the presence or absence PMA (3 ng/ml). The effect of U0126 was examined. ^{35}S-Labeled GATA3 protein was visualized by autoradiography. Arbitrary densitometric units are shown below each band. Three independent experiments were performed, and a representative result is shown. *D*, effect of an active form of ERK2 (Erk2 sem) and a dominant-negative form of ERK2 (dnErk2) on the expression of GATA3. Splenic CD4 T cells were stimulated as described in *A*, and the cells were infected with retrovirus encoding ERK2 mutant bicistronically with human coxsackievirus and adenovirus receptor (*CAR*). Three days after infection, the coxsackievirus and adenovirus receptor-positive population was enriched by MACS and cultured at 37 °C for 12 h without cytokines. Then the expression levels of GATA3 protein were assessed. Arbitrary densitometric units are shown below each band. Four independent experiments were performed, and a representative result is shown.

the cytosol, and treatment with either CHX or MG132 did not have a significant effect on the levels of the mutant protein. Small amounts of dZF protein were detected in the nuclear fraction, and a modest increase was detected in the presence of MG132. Thus it would appear the C-terminal region of GATA3, including the zinc finger region (residues 261–315), is critical for proteasome-dependent degradation.

To visualize the dynamics of localization and accumulation, green fluorescence protein (GFP)-fused wild type GATA3 and the dZF mutant were expressed in NIH3T3 cells. As expected, wild type GATA3 showed decreased fluorescence following CHX treatment, and the decrease in fluorescence was prevented to some extent in the presence of MG132 (supplemental Fig. 1). The dZF mutant was expressed in both nuclear and cytosolic fractions, and the fluorescence intensity was not affected by treatment with CHX or MG132. These results are consistent with the results shown in Fig. 4*C*.

The ERK MAPK Cascade Regulates GATA3 Ubiquitination—In order to assess the involvement of multiubiquitination (Ub) in GATA3 degradation, FLAG-tagged wild type GATA3, dCT, dCF, and dZF mutants were each transfected into 293T cells, and transfectants were treated with MG132. Immuno-

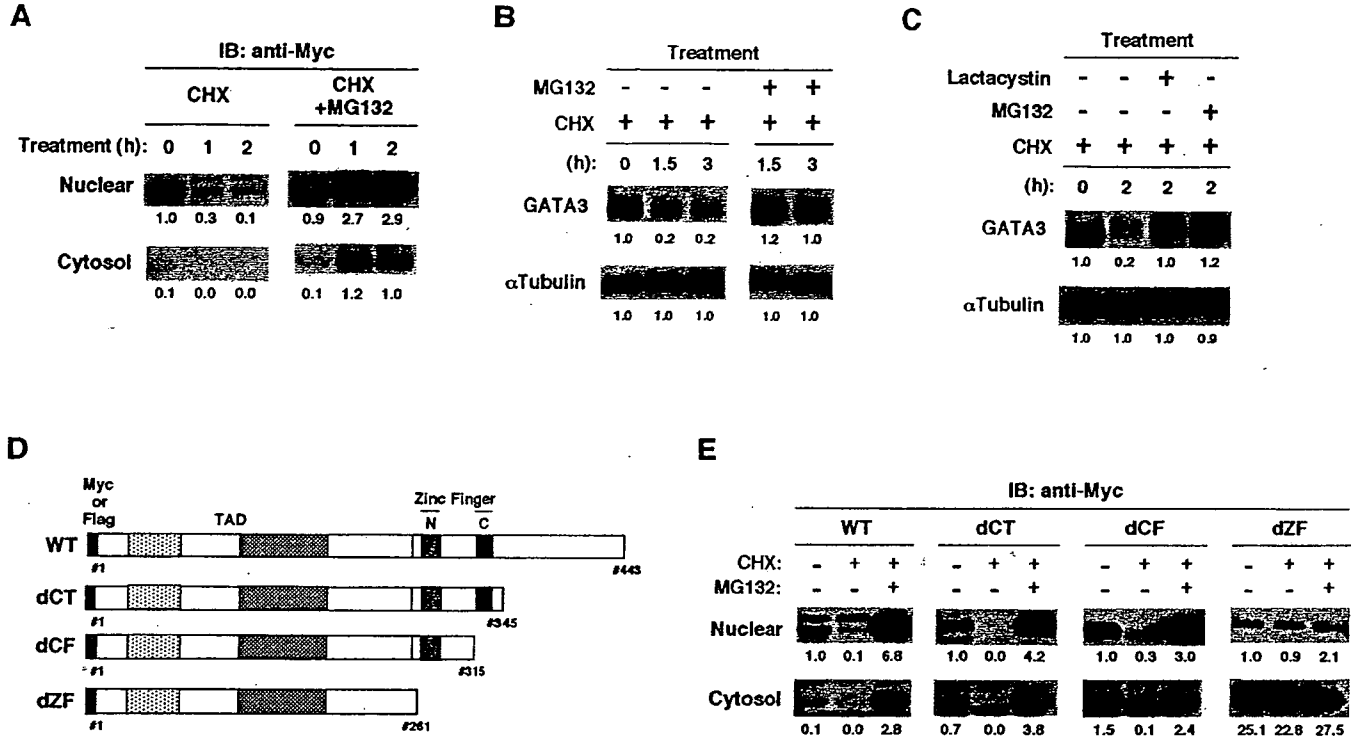

FIG. 4. **GATA3 is rapidly degraded via a 26 S proteasome-dependent pathway.** *A*, GATA3 is degraded in a 26 S proteasome-dependent manner. Myc-tagged GATA3 was introduced into COS cells. The transfected cells were harvested at the indicated time after treatment with cycloheximide (100 μM) and proteasome inhibitor MG132 (50 μM). Nuclear and cytoplasmic extracts were prepared, and the amount of Myc-tagged GATA3 was assessed by immunoblotting (*IB*) with anti-Myc mAb. Arbitrary densitometric units are shown below each band. *B*, splenic CD4 T cells were stimulated under Th2− conditions for 4 days. The cells were then treated with CHX (100 μM) in the presence or absence of MG132 (20 μM) for the indicated times. Total cell extracts were prepared using RIPA lysis buffer. The amount of GATA3 protein was assessed by immunoblotting with anti-GATA3 mAb. Arbitrary densitometric units are shown below each band. *C*, developing Th2 cells prepared as in *B* were treated with CHX (100 μM) in the presence or absence of MG132 (20 μM) or lactacystin (20 μM) for 2 h. The amount of GATA3 protein was assessed as in *B*. *D*, schematic representation of Myc-tagged GATA3 mutants. Wild type GATA3 (*WT*) and three mutants (*dCT*, *dCF*, and *dZF*) are shown with the location of the Myc tag (*Myc*), the transactivation domain (*TAD*), and the two zinc finger domains (*N* and *C*). *E*, degradation and MG132-induced rescue of GATA3 mutants. Myc-tagged GATA3 mutants were transfected into COS7 cells, and the transfectants were treated with the indicated inhibitors for 2 h. The amounts of Myc-tagged GATA3 were assessed as in *A*. Arbitrary densitometric units are shown below each band. Four independent experiments were performed with similar results.

blotting with anti-Ub mAb was performed after anti-FLAG immunoprecipitation (Fig. 5*A*). Significantly increased levels of multiubiquitination (appears as smear) were observed in the wild type GATA3 transfectants compared with control vector, and the levels were significantly increased in the presence of MG132 (Fig. 5*A*, compare *lanes 3* and *4*). The levels of multiubiquitination appeared to be equivalent in the case of the dCT mutant (Fig. 5*A*, *lanes 5* and *6*), slightly decreased in the dCF mutant (*lanes 7* and *8*), and greatly reduced in the dZF mutant (*lanes 9* and *10*). The levels of FLAG-tagged protein in total (nuclear and cytoplasmic) lysates were not reduced in these transfectants (Fig. 5*A*, *right panel*). Thus, multiubiquitination of GATA3 protein can be readily demonstrated, and it appears that the dZF mutant is the least modified among the mutant forms tested. The multiubiquitination on truncated GATA3 mutants was further assessed by anti-FLAG immunoblotting (Fig. 5*B*). The levels of multiubiquitination were slightly decreased in the dCF mutant and greatly reduced in the dZF mutant, indicating again that the C-terminal region of GATA3, including the zinc finger region (residues 261–315), is critical for ubiquitination.

We performed an *in vitro* ubiquitination assay as a further demonstration of the multiubiquitination on GATA3. 293T cells were transfected with FLAG-tagged GATA3, and 3 days later, the cells were treated with MG132 for 2 h. *In vitro* ubiquitination was performed after anti-GATA3 immunoprecipitation, and ubiquitinated GATA3 was detected by immunoblotting with anti-GATA3 (Fig. 5*C*, *left panel*). Concurrently, anti-FLAG immunoprecipitation and anti-FLAG immunoblotting were done (Fig. 5*C*, *right*). Although variable levels of multiubiquitinated GATA3 were detected without *in vitro* ubiquitination (Fig. 5*C*, *lane 4*), significantly increased signals with new bands (indicated by *) were detected after *in vitro* ubiquitination (*lane 8*). Similarly, increased ubiquitination was readily detected after *in vitro* ubiquitination in the anti-FLAG immunoblot (Fig. 5*C*, compare *lanes 12* and *14*).

Next, in order to examine the involvement of activation of the ERK-MAPK cascade in the GATA3 ubiquitination, we assessed the effect of PMA to activate the MAPK cascades and U0126 to inhibit selectively the ERK-MAPK cascade on the ubiquitination of GATA3. 293T cells transfected with FLAG-tagged GATA3 were treated with PMA in the presence or absence of U0126, and then the levels of ubiquitination on GATA3 were assessed (Fig. 5*D*). Treatment with PMA resulted in a reduction in the degree of ubiquitination of GATA3, and this effect could be reversed significantly by the addition of U0126, suggesting that the ubiquitination of GATA3 is regulated by the activation of ERK MAPK. Similarly, in developing Th2 cells, the ubiquitination of GATA3 protein was detected when the cells were treated with MG132 (20 μM) for 2 h, and the levels in ubiquitination were enhanced in the presence of U0126 (data not shown).

Mdm2 Acts as a Ubiquitin E3 Ligase for GATA3—We wanted to identify possible E3 ligase for GATA3 in developing Th2 cells. Since the association with specific substrates is critical for the function of E3 ligases (32, 45), we first examined the physical association of GATA3 with known E3 ligases that are expressed in lymphocytes (Mdm2, Itch, E6-AP, and Cbl-b).

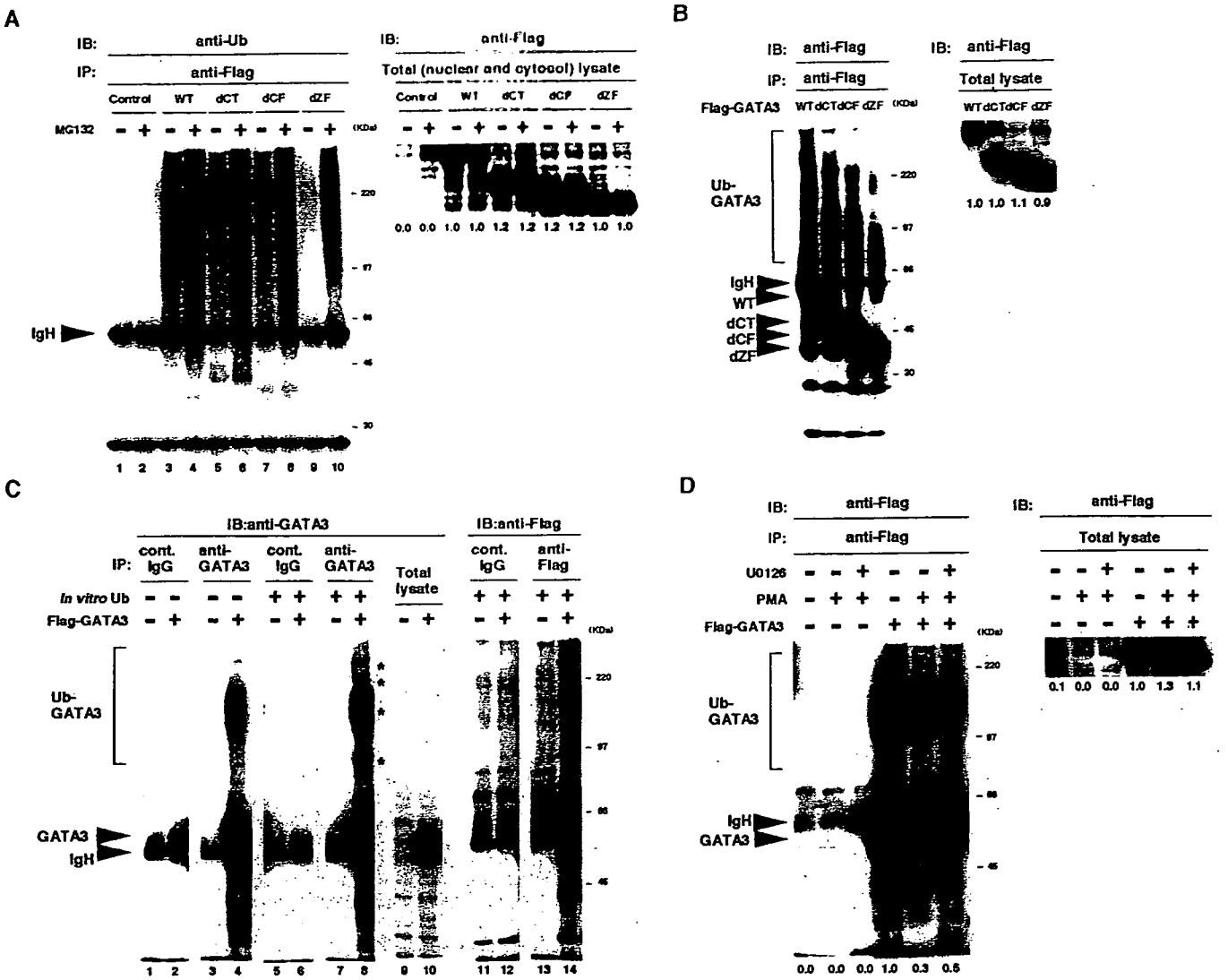

FIG. 5. **GATA3 was ubiquitinated *in vivo* and *in vitro*.** *A*, ubiquitination of GATA3 *in vivo*. 293T cells were transfected with expression plasmids encoding FLAG-tagged GATA3 wild type (*WT*) and mutants (*dCT*, *dCF*, and *dZF*), and 72 h later were treated with MG132 (50 μM) for 2 h. FLAG-tagged GATA3 was immunoprecipitated (*IP*) with anti-FLAG mAb, and the level of ubiquitination was assessed by immunoblotting (*IB*) with anti-Ub mAb (*left panel*). The levels of FLAG-tagged transfected protein in the total (nuclear and cytoplasmic) lysates were also assessed by anti-FLAG immunoblotting (*right panel*). Arbitrary densitometric units are shown below each lane. *B*, FLAG-tagged GATA3 mutants were immunoprecipitated with anti-FLAG mAb, and the levels of ubiquitination were visualized by immunoblotting with anti-FLAG mAb. The positions of migration of ubiquitinated GATA3 (*Ub-GATA3*), nonubiquitinated GATA3 wild type (*WT*), and mutants (*WT*, *dCT*, *dCF*, and *dZF*), and IgH are indicated. Total (nuclear and cytoplasmic) lysates (3 μl) were also run in parallel. Arbitrary densitometric units are shown below each lane. *C*, ubiquitination of GATA3 *in vitro*. 293T cells were transfected with FLAG-tagged GATA3, and 72 h later the cells were treated with MG132 (50 μM) for 2 h. Immunoprecipitates with anti-GATA3 or anti-FLAG mAb were subjected to *in vitro* ubiquitination assay. Ubiquitinated GATA3 was visualized by immunoblotting with anti-GATA3 or anti-FLAG mAb. The positions of migration of ubiquitinated GATA3 (*Ub-GATA3*), nonubiquitinated GATA3 (*GATA3*), and IgH are indicated. The Ub-GATA3 bands that appeared after *in vitro* ubiquitination are indicated by *asterisks*. Total lysates (10 μl) were also run in parallel. *D*, ERK-MAPK cascade controls GATA3 ubiquitination. 293T cells were transfected with FLAG-tagged GATA3. Three days after transfection, the cells were treated with PMA (10 ng/ml) and U0126 (20 μM) for 3 h and then treated with MG132 (50 μM) for 2 h. GATA3 was immunoprecipitated with anti-FLAG mAb and visualized with anti-FLAG immunoblotting. Arbitrary densitometric units of the major Ub-GATA3 band are shown below each lane. Total lysates (3 μl) were also run in parallel.

Freshly isolated splenic CD4 T cells were stimulated with immobilized anti-TCR mAb under Th2− conditions for 3 days in the presence or absence of U0126. Immunoprecipitates with anti-GATA3 mAb were subjected to immunoblotting with anti-Mdm2 mAb and anti-GATA3 mAb (Fig. 6*A*) and with specific antibodies for several E3 ligases (Fig. 6*B*). Large amounts of Mdm2 were detected in the GATA3− precipitates from U0126-treated cells, suggesting association of Mdm2 with GATA3, although the amount of GATA3 is significantly reduced (~1/3) in the U0126-treated cells (Fig. 6*A*). Although there were substantial amounts of E6-AP, Itch, or Cbl-b molecules in developing Th2 cells, no significant quantity of E6-AP, Itch, or Cbl-b was detected in the anti-GATA3 immunoprecipitates under the conditions where substantial amounts of Mdm2 were detected (Fig. 6*B*). Thus, the association of Mdm2 with GATA3 appeared to be more selective than that of other E3 ligases (Itch, E6-AP, and Cbl-b).

To characterize further the Mdm2 association with GATA3, 293T cells were transfected with FLAG-tagged GATA3 and their mutants (dCT, dCF, and dZF) and were treated with MG132 for 2 h. Immunoprecipitates with anti-FLAG mAb were immunoblotted with anti-Mdm2 mAb. As shown in Fig. 6*B*, *upper panel*, association of Mdm2 with GATA3 was readily detected, and the association was apparently decreased in the dCF mutant and almost undetectable in the dZF mutant. The amounts of Mdm2 and FLAG-GATA3 protein in these transfectants were similar (Fig. 6*B*, *middle* and *bottom panels*). Thus Mdm2 appears to be constitutively associated with wild type

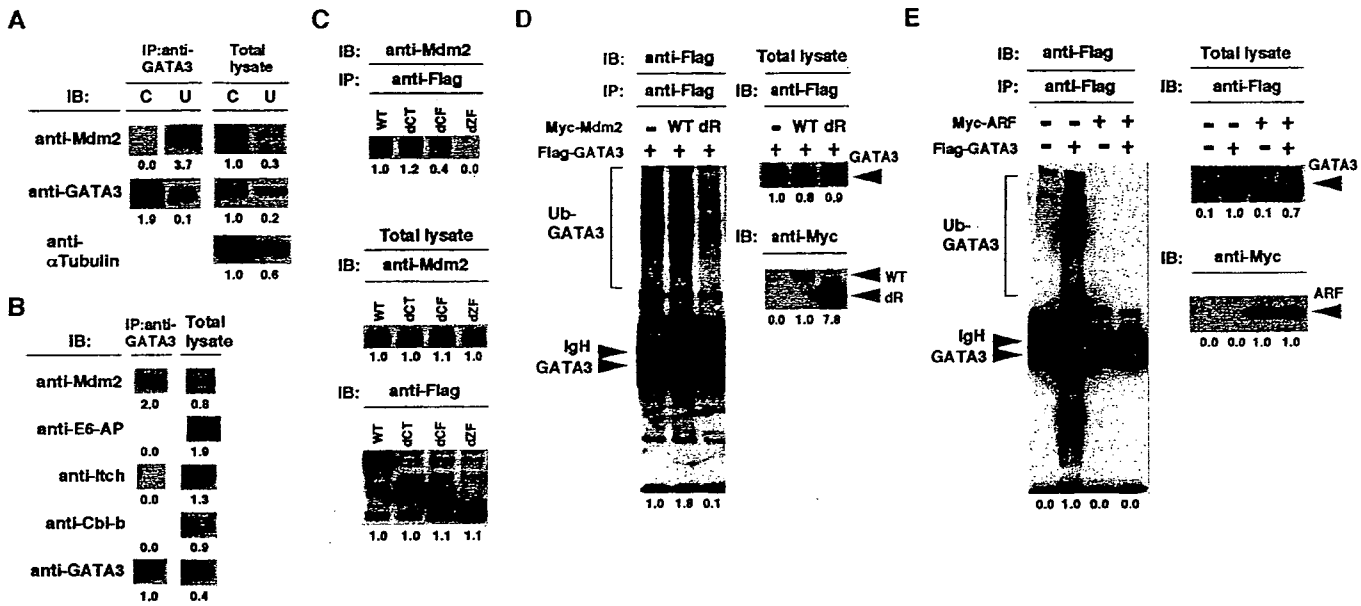

FIG. 6. **Mdm2 acts as an E3 ligase for GATA3.** *A*, Mdm2 is associated with GATA3 in developing Th2 cells. Splenic CD4T cells were cultured under Th2− conditions for 3 days in the presence (*U*) or absence (*C*) of U0126 (20 μM). Immunoprecipitates with anti-GATA3 mAb from the cultured cells were subjected to immunoblotting (*IB*) with anti-Mdm2 and anti-GATA3. Total lysates were also run in parallel. Arbitrary densitometric units are shown below each band. *B*, splenic CD4T cells were cultured under Th2− conditions for 3 days in the presence of U0126 (20 μM). Immunoprecipitates with anti-GATA3 mAb were subjected to immunoblotting with anti-Mdm2, anti-E6-AP, anti-Itch, anti-Cbl-b, and anti-GATA3 antibodies. Total lysates were also run in parallel. Arbitrary densitometric units are shown below each band. *C*, Mdm2 is associated with GATA3 in 293T cells. 293T cells were transfected with FLAG-tagged GATA3 and mutants (*dCT*, *dCF*, and *dZF*). Three days after transfection, cells were treated with MG132 (50 μM) for 2 h. Immunoprecipitates (*IP*) with anti-FLAG mAb were immunoblotted with anti-Mdm2 mAb. Total lysates (10 μl) were run in parallel. Arbitrary densitometric units of the band are shown below each band. *D*, Mdm2 acts as E3 ligase for GATA3. 293T cells were transfected with FLAG-tagged GATA3 and Myc-tagged wild type (*WT*) Mdm2 or Myc-tagged RING finger-deleted Mdm2. Three days after transfection, cells were treated with MG132 (50 μM) for 2 h. Immunoprecipitates with an anti-FLAG mAb were subjected to immunoblotting with anti-Myc mAb. The positions of migration of ubiquitinated GATA3 (*Ub-GATA3*), nonubiquitinated GATA3 (*GATA3*), IgH, and Myc-tagged wild type Mdm2 (*WT*) and Myc-tagged RING finger-deleted Mdm2 (*dR*) are indicated. Arbitrary densitometric units of the major Ub-GATA3 band are shown below each lane. *E*, overexpression of ARF suppressed multiubiquitination of GATA3. 293T cells were transfected with FLAG-tagged GATA3 and Myc-tagged ARF. FLAG-tagged GATA3 were immunoprecipitated with anti-FLAG mAb, and the levels of ubiquitination were visualized by immunoblotting with anti-FLAG mAb. Transfected Myc-tagged ARF was detected by immunoblotting with anti-Myc mAb. The positions of migration of ubiquitinated GATA3 (*Ub-GATA3*), nonubiquitinated GATA3 (*GATA3*), IgH and Myc-tagged ARF (*ARF*) are indicated. Arbitrary densitometric units of the major Ub-GATA3 band are shown below each lane.

GATA3 in 293T cells, and the C-terminal region including the zinc finger domain is important for association.

To assess whether Mdm2 has E3 ligase activity for GATA, FLAG-tagged GATA3 and Myc-tagged wild type and a RING finger-deleted Mdm2 were expressed in 293T cells. The RING finger domain of Mdm2 is critical for E3 ligase activity for p53 (46). Immunoprecipitates with an anti-FLAG mAb were subjected to immunoblotting with anti-FLAG mAb. Overexpression of wild type Mdm2 led to increased levels of multiubiquitination of GATA3 (Fig. 6*C*, *1st two lanes*). More interestingly, the ubiquitination of GATA3 was greatly reduced when the RING finger-deleted Mdm2 was expressed. The levels were much lower than those in cells without Mdm2 transfection, suggesting a dominant-negative feature of the RING finger-deleted Mdm2 to endogenously expressing Mdm2 in 293T cells. The efficiency of expression of the transfected RING finger-deleted Mdm2 was considerably high (Fig. 6*C*, *right panel*), probably because of the inhibition of ubiquitination itself (47, 48).

It is known that cyclin-dependent kinase inhibitor 2A, a tumor suppressor molecule ($p19^{ARF}$ in the mouse and $p14^{ARF}$ in human cells), binds tightly to Mdm2 and prevents Mdm2-mediated p53 ubiquitination (49). Consequently, we tested the effect of expression of ARF in the GATA3 ubiquitination. As shown in Fig. 6*D*, *left panel*, the introduction of ARF resulted in nearly complete inhibition of the multiubiquitination of GATA3 in 293T cells. Collectively, these results support the notion that Mdm2 has E3 ligase activity for GATA3.

Mdm2 Is Involved in GATA3 Ubiquitination in T Cells—In order to provide additional evidence to support the role of Mdm2 as a major E3 ligase, we attempted the inhibition of GATA3 ubiquitination in T cells by using Mdm2 RNA interference. Mdm2 siRNA was introduced in a T cell line TG40 at a high level. The expression levels of Mdm2 protein were reduced significantly upon the introduction of the Mdm2 siRNA as compared with the control (Fig. 7*A*, *right top panel*). As anticipated, GATA3 ubiquitination was reduced substantially by the Mdm2 siRNA treatment (Fig. 7*A*, *left panel*, *lane 1.0 versus 0.4*). These results help to confirm the involvement of Mdm2 in GATA3 ubiquitination in TG40 T cells.

Finally, we wanted to address the function of Mdm2 in primary developing Th2 cells. The mRNA expression of Mdm2 was similar between developing Th1 and Th2 cells (data not shown). Our attempts to silence Mdm2 by RNA interference were unsuccessful with the primary T cells, probably because of robust proliferation of developing Th2 cells in the *in vitro* cultures. Thus we took an alternative approach to inhibit GATA3 ubiquitination and to facilitate Th2 cell differentiation by introducing a RING finger-deleted Mdm2 (Mdm2-dR) into developing Th2 cells (Fig. 7, *B* and *C*). There was substantial expression of endogenous Mdm2 in primary developing Th2 cells, and furthermore, the level of introduced Mdm2-dR by a retrovirus vector was lower than that of endogenous Mdm2 (Fig. 7*B*, *right top panel*). Nevertheless, GATA3 ubiquitination was significantly reduced (Fig. 7*B*, *left panel*, *lane1.0 versus 0.6*). Moreover, there was significant increase in the generation of IL-4-producing Th2 cells (38.4 *versus* 54.0%) with higher mean fluorescence intensity in IL-4 fluorescence (114.3 *versus* 163.6) when Mdm2-dR was expressed in developing Th2 cells (Fig. 7*C*). Thus, we conclude that Mdm2 is involved in GATA3

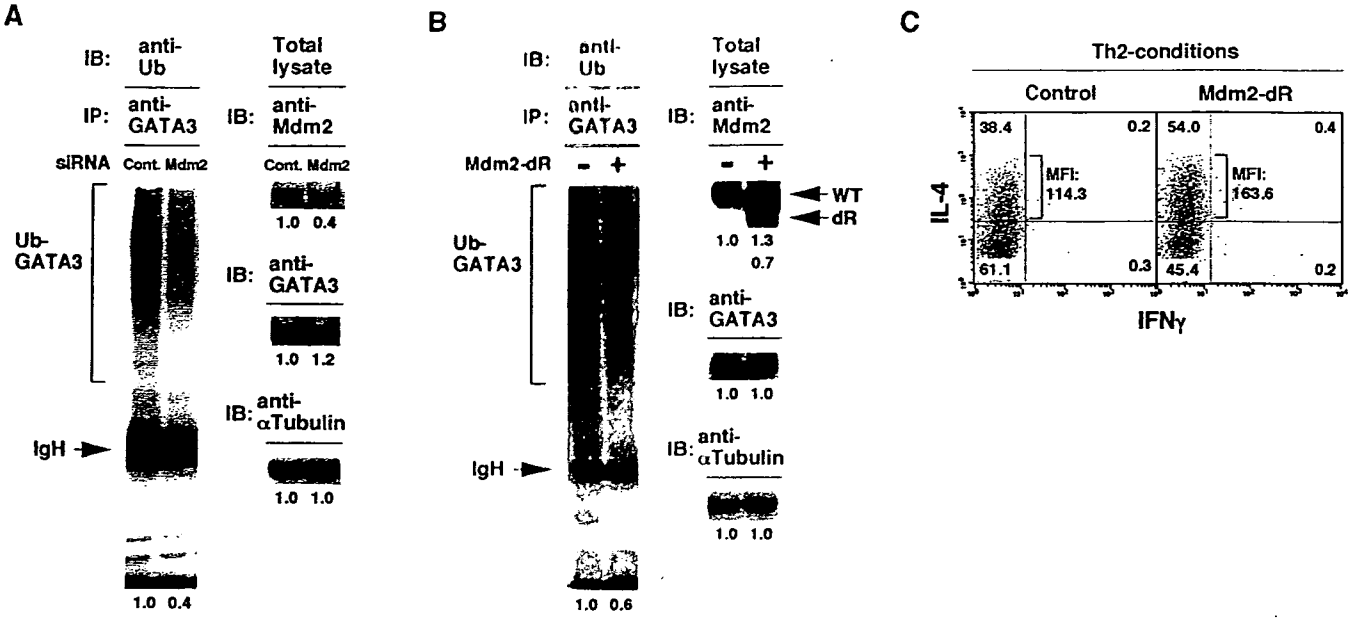

FIG. 7. **Mdm2 is involved in the ubiquitination of GATA3 in T cells.** *A*, inhibition of GATA3 ubiquitination with siRNA for Mdm2. Mouse T cell line TG40 cells were transfected with siRNA specific for Mdm2. Three days after transfection, cells were cultured at 37 °C for 2 h in the presence of MG132 (20 μM). Then the ubiquitination of GATA3 was assessed. Arbitrary densitometric units of the major Ub-GATA3 band are shown below each lane. The expression of Mdm2, GATA3, and α-tubulin is shown on the *right panels*. *IP*, immunoprecipitation; *IB*, immunoblot. *B*, effect of a dominant-negative (Ring-finger deleted) form of Mdm2 (*Mdm2-dR*) on the ubiquitination of GATA3 in developing Th2 cells. Splenic CD4 T cells were stimulated as described in Fig. 1, and the cells were infected with retrovirus encoding Mdm2 mutant bicistronically with human NGFR. Three days after infection, the NGFR-positive population was enriched by MACS and cultured at 37 °C for 2 h in the presence of MG132 (20 μM). Then the ubiquitination of GATA3 was assessed. Arbitrary densitometric units of the major Ub-GATA3 band are shown below each lane. The expression of Mdm2 (WT and dR), GATA3, and α-tubulin is shown on the *right panels*. *C*, expression of dominant-negative Mdm2 enhanced Th2 cell development. Freshly prepared splenic CD4 T cells were stimulated under Th2− skewed conditions and infected with retrovirus encoding Mdm2-dR bicistronically with EGFP on day 2. Three days later, the cells were stimulated with anti-TCR and were subjected to cytoplasmic IFNγ/IL-4 staining. Mean fluorescence intensity (*MFI*) of IL-4-staining is also indicated.

ubiquitination in primary Th2 cells and control Th2 cell differentiation.

DISCUSSION

In this paper, we provide evidence indicating that TCR-mediated activation of the Ras-ERK MAPK cascade controls GATA3 protein stability through the ubiquitin-proteasome pathway. The induction of GATA3 protein in developing Th2 cells is crucial for the differentiation of Th2 cells (18, 19). IL-4-induced STAT6 activation initiates transcription of GATA3 (50). However, among the issues that remain to be clarified is how the expression of GATA3 protein is controlled in developing Th2 cells. Here we demonstrate the following. (i) GATA3 protein is very unstable with a short half-life (~1 h) in transfectants (Fig. 4*A*) and developing Th2 cells (Fig. 4*B*). (ii) The degradation of GATA3 is dependent on the 26 S proteasome pathway (Fig. 4, *A–C*). (iii) GATA3 is ubiquitinated both *in vivo* and *in vitro* (Fig. 5). (iv) The deletion of the possible ubiquitination sites of GATA3 led to stable expression of GATA3 and reduced ubiquitination (Fig. 4*E* and Fig. 5, *A* and *B*). From these results, we conclude that the fate of GATA3 in developing Th2 is highly dependent on degradation through the ubiquitin-proteasome system. Concurrently, we show that activation of the ERK-MAPK cascade facilitated GATA3-mediated chromatin remodeling at the Th2 cytokine gene loci (Fig. 1) and inhibited the degradation (Figs. 2 and 3) and ubiquitination of the GATA3 molecule (Fig. 5*D*). Because the Ras-ERK MAPK cascade in naive CD4 T cells is activated by stimulation of TCR and not of IL-4R (11), the activation of the Ras-ERK MAPK cascade detected in the experiments must be a consequence of TCR-mediated signaling. Therefore, stabilization of GATA3 by the activation of the Ras-ERK MAPK cascade could be the mechanism that accounts for an essential role for TCR-mediated signaling in Th2 cell differentiation.

Our studies identify Mdm2 as a possible E3 ligase for GATA3. Mdm2 was shown to be associated with GATA3 in developing Th2 cells and 293T cells (Fig. 6, *A–C*). The overexpression of wild type Mdm2 induced increased ubiquitination on GATA3, whereas that of RING finger-deleted mutant Mdm2 resulted in the inhibition of GATA3 ubiquitination in 293T cells (Fig. 6*D*). Overexpression of ARF, an inhibitor of Mdm2, resulted in almost complete suppression of multiubiquitination of GATA3 in 293T cells (Fig. 6*E*). Moreover, the introduction of siRNA for Mdm2 into the T cell line TG40 resulted in the reduction in the ubiquitination of GATA3 protein (Fig. 7*A*). The generation of IL-4-producing Th2 cell was enhanced by the expression of RING finger-deleted mutant Mdm2, suggesting a physiological role for Mdm2 in Th2 cell differentiation (Fig. 7*C*).

Mdm2 is known to promote degradation of p53 through a ubiquitin-dependent proteasome pathway (49, 51). Mdm2 acts as an E3 ubiquitin ligase specific for p53 *in vitro* (51). The RING finger domain of Mdm2 is critical for E3 ligase activity for p53 (46). The phosphorylation of p53 at serine 15, threonine 18, and serine 20 led to the reduction of Mdm2 binding and enhancement of p53 stabilization and accumulation (49). Most interestingly, amino acid residues 9–20 (**SVEPPLSQETFS**) of human p53, which are reported to be important for the binding for Mdm2, are highly homologous to amino acid residues 131–142 of human GATA3 (**SVYPPASSSSLS**) and mouse GATA3 (**SVYPPASSSSLA**). In these regions, serine/threonine phosphorylation sites and surrounding proline residues (indicated in boldface above) occur in similar patterns between p53 and GATA3. Moreover, GATA3 has other structural similarities with p53, *e.g.* possible lysine ubiquitination sites at the C-terminal region (364–390 in p53 and 396–422 in GATA3) and a proline-rich regulatory region (69–101 in p53 and 146–178 in

GATA3), which are reported to have important roles in post-translational modification and functions of p53 (52, 53). Thus, it is reasonable to expect that a similar set of molecular events operating in ubiquitination of p53 would occur in the case of GATA3

In our experiments with truncation mutants, truncation of the above-mentioned lysine ubiquitination sites in the C-terminal region 396–422 in GATA3 (dCT mutant) resulted in small effects on degradation (Fig. 4*E*) and multiubiquitination of GATA3 (Fig. 5, *A* and *B*). A small but significant effect was observed in the dCF mutant (Fig. 5, *A* and *B*). A more prominent effect was observed by deletion of residues 261–443 (dZF mutant) (Fig. 4*E* and Fig. 5, *A* and *B*). The 261–315 region contains three lysine residues (293, 303, and 305 in human GATA3) and a nuclear localization signal (KPKRR). It is known that the degradation of p53 is controlled also by the localization of p53 and Mdm2 (54, 55). Thus, similar to p53, the degradation of GATA3 appears to be controlled by both the ubiquitination process and nuclear/cytosol localization of the protein.

The Ras-ERK MAPK cascade regulates stability of various proteins, including Myc, MKP-1, ATF2, and p53 through a mechanism involving serine phosphorylation (56–61). In addition, ERK MAPK-dependent phosphorylation and the subsequent enhancement of the transcriptional activities for GATA2 and GATA4 have been suggested (62, 63). GATA3 was phosphorylated by activated p38 MAPK in cAMP-treated T cells, suggesting a possible regulatory role for the MAPK cascade in GATA3 function (64). In fact, our preliminary results indicate that an active form of ERK2 directly phosphorylates GATA3 protein *in vitro*, and PMA-induced GATA3 phosphorylation was significantly inhibited by U0126 in transfected COS7 cells.[2] GATA3 protein contains numerous Ser/Thr residues (93 residues out of 444 residues) and possesses 35 putative phosphorylation sites, and thus the precise location of critical amino acid residues responsible for the MAPK-dependent phosphorylation remains unclear at this time. Thus, it appears to be reasonable to surmise that the activation of the ERK-MAPK cascade induces GATA3 phosphorylation and prevents its ubiquitin-mediated degradation through the 26 S proteasome.

Our studies with primary T cells indicated that the ERK-MAPK cascade plays a major role in the regulation of GATA3 protein expression. Although we observed the activation of the p38 MAPK cascade after PMA treatment in developing Th2 cells,[2] a specific inhibitor for the p38 MAPK cascade (SB203580) did not affect the GATA3 protein expression. However, it is still possible that the activation of the p38 MAPK cascade may have some effect on the expression of GATA3 protein as well as the function of GATA3 (64).

In summary, TCR-mediated activation of the Ras-ERK MAPK cascade controls the stability of GATA3 protein by a ubiquitin-proteasome-dependent mechanism. IL-4-induced STAT6 activation is required for the induction of GATA3 transcription. Thus, efficient activation of both signaling pathways and resulting stable GATA3 expression, therefore, are crucial for chromatin remodeling at the Th2 cytokine gene loci and successful Th2 cell differentiation.

Acknowledgments—We are grateful to Dr. Ralph T. Kubo for helpful comments and constructive criticisms in the preparation of the manuscript. We also thank Dr. Keiji Tanaka for helpful comments and reagents for the ubiquitination assay. We thank Maki Ukai-Tadenima, Kaoru Sugaya, and Satoko Norikane for their excellent technical assistance.

REFERENCES

1. Mosmann, T. R., and Coffman, R. L. (1989) *Adv. Immunol.* **46**, 111–147
2. Seder, R. A., and Paul, W. E. (1994) *Annu. Rev. Immunol.* **12**, 635–673
3. Reiner, S. L., and Locksley, R. M. (1995) *Annu. Rev. Immunol.* **13**, 151–177
4. Abbas, A. K., Murphy, K. M., and Sher, A. (1996) *Nature* **383**, 787–793
5. Constant, S. L., and Bottomly, K. (1997) *Annu. Rev. Immunol.* **15**, 297–322
6. O'Garra, A. (1998) *Immunity* **8**, 275–283
7. Gately, M. K., Renzetti, L. M., Magram, J., Stern, A. S., Adorini, L., Gubler, U., and Presky, D. H. (1998) *Annu. Rev. Immunol.* **16**, 495–521
8. Murphy, K. M., Ouyang, W., Farrar, J. D., Yang, J., Ranganath, S., Asnagli, H., Afkarian, M., and Murphy, T. L. (2000) *Annu. Rev. Immunol.* **18**, 451–494
9. Nelms, K., Keegan, A. D., Zamorano, J., Ryan, J. J., and Paul, W. E. (1999) *Annu. Rev. Immunol.* **17**, 701–738
10. Yamashita, M., Hashimoto, K., Kimura, M., Kubo, M., Tada, T., and Nakayama, T. (1998) *Int. Immunol.* **10**, 577–591
11. Yamashita, M., Kimura, M., Kubo, M., Shimizu, C., Tada, T., Perlmutter, R. M., and Nakayama, T. (1999) *Proc. Natl. Acad. Sci. U. S. A.* **96**, 1024–1029
12. Yamashita, M., Katsumata, M., Iwashima, M., Kimura, M., Shimizu, C., Kamata, T., Shin, T., Seki, N., Suzuki, S., Taniguchi, M., and Nakayama, T. (2000) *J. Exp. Med.* **191**, 1869–1879
13. Shibata, Y., Kamata, T., Kimura, M., Yamashita, M., Wang, C. R., Murata, K., Miyazaki, M., Taniguchi, M., Watanabe, N., and Nakayama, T. (2002) *J. Immunol.* **169**, 2134–2140
14. Dong, C., Yang, D. D., Wysk, M., Whitmarsh, A. J., Davis, R. J., and Flavell, R. A. (1998) *Science* **282**, 2092–2095
15. Yang, D. D., Conze, D., Whitmarsh, A. J., Barrett, T., Davis, R. J., Rincon, M., and Flavell, R. A. (1998) *Immunity* **9**, 575–585
16. Rengarajan, J., Szabo, S. J., and Glimcher, L. H. (2000) *Immunol. Today* **21**, 479–483
17. Zhang, D. H., Cohn, L., Ray, P., Bottomly, K., and Ray, A. (1997) *J. Biol. Chem.* **272**, 21597–21603
18. Zheng, W., and Flavell, R. A. (1997) *Cell* **89**, 587–596
19. Ouyang, W., Ranganath, S. H., Weindel, K., Bhattacharya, D., Murphy, T. L., Sha, W. C., and Murphy, K. M. (1998) *Immunity* **9**, 745–755
20. Lee, H. J., Takemoto, N., Kurata, H., Kamogawa, Y., Miyatake, S., O'Garra, A., and Arai, N. (2000) *J. Exp. Med.* **192**, 105–115
21. Yamashita, M., Ukai-Tadenuma, M., Miyamoto, T., Sugaya, K., Hosokawa, H., Hasegawa, A., Kimura, M., Taniguchi, M., DeGregori, J., and Nakayama, T. (2004) *J. Biol. Chem.* **279**, 26983–26990
22. Pai, S. Y., Truitt, M. L., and Ho, I. C. (2004) *Proc. Natl. Acad. Sci. U. S. A.* **101**, 1993–1998
23. Yamashita, M., Ukai-Tadenuma, M., Kimura, M., Omori, M., Inami, M., Taniguchi, M., and Nakayama, T. (2002) *J. Biol. Chem.* **277**, 42399–42408
24. Avni, O., Lee, D., Macian, F., Szabo, S. J., Glimcher, L. H., and Rao, A. (2002) *Nat. Immun.* **3**, 643–651
25. Fields, P. E., Kim, S. T., and Flavell, R. A. (2002) *J. Immunol.* **169**, 647–650
26. Inami, M., Yamashita, M., Tenda, Y., Hasegawa, A., Kimura, M., Hashimoto, K., Seki, N., Taniguchi, M., and Nakayama, T. (2004) *J. Biol. Chem.* **279**, 23123–23133
27. Omori, M., Yamashita, M., Inami, M., Ukai-Tadenuma, M., Kimura, M., Nigo, Y., Hosokawa, H., Hasegawa, A., Taniguchi, M., and Nakayama, T. (2003) *Immunity* **19**, 281–294
28. Tanaka, K., and Chiba, T. (1998) *Genes Cells* **3**, 499–510
29. Ciechanover, A. (1998) *EMBO J.* **17**, 7151–7160
30. Laney, J. D., and Hochstrasser, M. (1999) *Cell* **97**, 427–430
31. Ben-Neriah, Y. (2002) *Nat. Immun.* **3**, 20–26
32. Liu, Y. C. (2004) *Annu. Rev. Immunol.* **22**, 81–127
33. Rock, K. L., and Goldberg, A. L. (1999) *Annu. Rev. Immunol.* **17**, 739–779
34. Karin, M., and Ben-Neriah, Y. (2000) *Annu. Rev. Immunol.* **18**, 621–663
35. Takeda, K., Tanaka, T., Shi, W., Matsumoto, M., Minami, M., Kashiwamura, S., Nakanishi, K., Yoshida, N., Kishimoto, T., and Akira, S. (1996) *Nature* **380**, 627–630
36. Swan, K. A., Alberola-Ila, J., Gross, J. A., Appleby, M. W., Forbush, K. A., Thomas, J. F., and Perlmutter, R. M. (1995) *EMBO J.* **14**, 276–285
37. Kimura, M., Koseki, Y., Yamashita, M., Watanabe, N., Shimizu, C., Katsumoto, T., Kitamura, T., Taniguchi, M., Koseki, H., and Nakayama, T. (2001) *Immunity* **15**, 275–287
38. Leon, R. P., Hedlund, T., Meech, S. J., Li, S., Schaack, J., Hunger, S. P., Duke, R. C., and DeGregori, J. (1998) *Proc. Natl. Acad. Sci. U. S. A.* **95**, 13159–13164
39. Oh-hora, M., Ogata, M., Mori, Y., Adachi, M., Imai, K., Kosugi, A., and Hamaoka, T. (1999) *J. Immunol.* **163**, 1282–1288
40. Iritani, B. M., Forbush, K. A., Farrar, M. A., and Perlmutter, R. M. (1997) *EMBO J.* **16**, 7019–7031
41. Favata, M. F., Horiuchi, K. Y., Manos, E. J., Daulerio, A. J., Stradley, D. A., Feeser, W. S., Van Dyk, D. E., Pitts, W. J., Earl, R. A., Hobbs, F., Copeland, R. A., Magolda, R. L., Scherle, P. A., and Trzaskos, J. M. (1998) *J. Biol. Chem.* **273**, 18623–18632
42. Suzuki, H., Chiba, T., Kobayashi, M., Takeuchi, M., Furuichi, K., and Tanaka, K. (1999) *Biochem. Biophys. Res. Commun.* **256**, 121–126
43. Lovett-Racke, A. E., Rocchini, A. E., Choy, J., Northrop, S. C., Hussain, R. Z., Ratts, R. B., Sikder, D., and Racke, M. K. (2004) *Immunity* **21**, 719–731
44. Li, Y. Q., Hii, C. S., Der, C. J., and Ferrante, A. (1999) *Immunology* **96**, 524–528
45. Pickart, C. M. (2004) *Cell* **116**, 181–190
46. Joazeiro, C. A., and Weissman, A. M. (2000) *Cell* **102**, 549–552
47. Honda, R., and Yasuda, H. (2000) *Oncogene* **19**, 1473–1476
48. Fang, S., Jensen, J. P., Ludwig, R. L., Vousden, K. H., and Weissman, A. M. (2000) *J. Biol. Chem.* **275**, 8945–8951
49. Michael, D., and Oren, M. (2003) *Semin. Cancer Biol.* **13**, 49–58
50. Ouyang, W., Lohning, M., Gao, Z., Assenmacher, M., Ranganath, S., Radbruch, A., and Murphy, K. M. (2000) *Immunity* **12**, 27–37
51. Honda, R., Tanaka, H., and Yasuda, H. (1997) *FEBS Lett.* **420**, 25–27

[2] M. Yamashita and T. Nakayama, unpublished observations.

52. Prives, C., and Manley, J. L. (2001) *Cell* **107**, 815–818
53. Brooks, C. L., and Gu, W. (2003) *Curr. Opin. Cell Biol.* **15**, 164–171
54. Tao, W., and Levine, A. J. (1999) *Proc. Natl. Acad. Sci. U. S. A.* **96**, 6937–6941
55. Li, M., Brooks, C. L., Wu-Baer, F., Chen, D., Baer, R., and Gu, W. (2003) *Science* **302**, 1972–1975
56. Sears, R., Nuckolls, F., Haura, E., Taya, Y., Tamai, K., and Nevins, J. R. (2000) *Genes Dev.* **14**, 2501–2514
57. Sears, R., Leone, G., DeGregori, J., and Nevins, J. R. (1999) *Mol. Cell* **3**, 169–179
58. Brondello, J. M., Pouyssegur, J., and McKenzie, F. R. (1999) *Science* **286**, 2514–2517
59. Fuchs, S. Y., Tappin, I., and Ronai, Z. (2000) *J. Biol. Chem.* **275**, 12560–12564
60. Persons, D. L., Yazlovitskaya, E. M., and Pelling, J. C. (2000) *J. Biol. Chem.* **275**, 35778–35785
61. She, Q. B., Chen, N., and Dong, Z. (2000) *J. Biol. Chem.* **275**, 20444–20449
62. Towatari, M., May, G. E., Marais, R., Perkins, G. R., Marshall, C. J., Cowley, S., and Enver, T. (1995) *J. Biol. Chem.* **270**, 4101–4107
63. Morimoto, T., Hasegawa, K., Kaburagi, S., Kakita, T., Wada, H., Yanazume, T., and Sasayama, S. (2000) *J. Biol. Chem.* **275**, 13721–13726
64. Chen, C. H., Zhang, D. H., LaPorte, J. M., and Ray, A. (2000) *J. Immunol.* **165**, 5597–5605